The Reaction Coordinate of a Functional Model of Tyrosinase: Spectroscopic and Computational Characterization

Bryan T. Op't Holt, **Michael A. Vance**, **Liviu M. Mirica**, **T. Daniel P. Stack**[*], and **Edward I. Solomon**[*]
Contribution from the Department of Chemistry, Stanford University, California 94305

Abstract

The μ-η^2:η^2-peroxodicopper(II) complex synthesized by reacting the Cu(I) complex of the bis-diamine ligand N,N′-di-*tert*-butyl-ethylenediamine (DBED) with O_2 is a functional and spectroscopic model of the coupled binuclear copper protein tyrosinase. This complex reacts with 2,4-di-*tert*-butylphenolate at low temperature to produce a mixture of the catechol and quinone products, which proceeds through three intermediates (**A – C**) that have been characterized. **A**, stabilized at 153K, is characterized as a phenolate-bonded bis-μ-oxo dicopper(III) species, which proceeds at 193K to **B**, presumably a catecholate-bridged coupled bis-copper(II) species via an electrophilic aromatic substitution mechanism wherein aromatic ring distortion is the rate-limiting step. Isotopic labeling shows that the oxygen inserted into the aromatic substrate during hydroxylation derives from dioxygen, and a late-stage *ortho*-H^+ transfer to an exogenous base is associated with C-O bond formation. Addition of a proton to **B** produces **C**, determined from resonance Raman spectra to be a Cu(II)-semiquinone complex. The formation of **C** (the oxidation of catecholate and reduction to Cu(I)) is governed by the protonation state of the distal bridging oxygen ligand of **B**. Parallels and contrasts are drawn between the spectroscopically and computationally supported mechanism of the DBED system, presented here, and the experimentally-derived mechanism of the coupled binuclear copper protein tyrosinase.

A. Introduction

The coupled binuclear copper proteins fulfill various important biological functions.[1–4] Hemocyanin (Hc) reversibly binds dioxygen in mollusks and arthropods; catechol oxidase (CO) binds dioxygen and oxidizes catechols to quinones as an injury response mechanism in plants. Tyrosinase (Ty), widely distributed in nature, reversibly binds dioxygen, hydroxylates monophenols to catechols, and performs the subsequent oxidation of catechols to quinones. Although these proteins exhibit different enzymatic functions, their spectroscopic properties[5] and crystallographic structures reveal striking electronic and geometric similarities among their active sites.[6–8] Upon O_2 binding, Hc, CO, and Ty all exhibit a characteristic side-on bridging μ-η^2:η^2 peroxodicopper(II) active site (**P**). In O_2-bonded Ty (oxyTy), the phenolic substrate binds directly to one Cu ion[9, 10] and is hydroxylated via a mechanism consistent with electrophilic aromatic substitution (EAS). In the spectroscopically determined mechanism for Ty activity, **P** is the only form of oxyTy observed,[5] and potential intermediates beyond **P** are unknown (Scheme 1).

The capability of oxyTy to activate and hydroxylate the *ortho*-C-H bond in a phenol is the most impressive function of coupled binuclear copper enzymes. This reactivity has motivated intense efforts by many groups to replicate synthetically the **P** complex[11, 12] and its ability to

Email: E-mail: Edward.solomon@stanford.edu.

hydroxylate substrates.[12–22] The first structurally characterized **P** complex was described by Kitajima *et al.* with the tridentate [Cu(HB-(3,5-iPr$_2$pz)$_3$)]$_2$(O$_2$) system, which exhibited similar electronic spectra as the Cu$_2$O$_2$ cores of O$_2$-bonded Hc and oxyTy that are known to be **P** species.[23] Karlin showed that a system with Py2-*m*-xyl^R ligands forms a **P** complex capable of hydroxylating an arene ring.[24–26] Tolman first described a new Cu$_2$/O$_2$ motif lacking an O-O bond,[27] a bis-μ-oxo dicopper(III) species (**O**),[28–31] which was in equilibrium with a **P** species.[32, 33] Stack and coworkers have used sterically-demanding diamine frameworks to produce equilibrium mixtures of **P** and **O**.[33]

In particular, reaction of the Cu(I) complex of N,N′-di-*tert*-butyl-ethylenediamine (DBED) with O$_2$ in aprotic solvent at 193K generates such a mixture, comprised of ~95% **P^{DBED}** and ~5% **O^{DBED}**, as elucidated by resonance Raman (rR) experiments on isotopically labeled complexes.[14, 16] The O$_2$-bonded dicopper DBED complex reacts with one to five equivalents of sodium 2,4-di-*tert*-butylphenolate at 193K to produce an ~1:1 ratio of 2,4-di-*tert*-butyl-1,2-benzoquinone and 2,4-di-*tert*-butyl-catechol. The spectroscopic and functional similarities of the **P^{DBED}** system to oxyTy invite a more detailed comparison. **P^{DBED}** reacts more slowly with electron-deficient aromatic phenolates, (Hammett ρ=−2.2), consistent with an EAS mechanism. The Hammett parameter for oxyTy is ρ=−2.4, suggesting that oxyTy also follows an EAS mechanism.[15]

The reaction of **P^{DBED}** with 2,4-di-*tert*-butylphenolate performed at 153K leads to the formation of Intermediate **A**,[15] a phenolate-bonded bis-μ-oxo dicopper(III) (an **O** species) complex that oxygenates the phenolate via subsequent intermediates **B** and **C** (*vide infra*). Each of these species is studied here spectroscopically, kinetically, and computationally to evaluate potential molecular mechanisms of phenolate hydroxylation. This study follows the electronic and structural changes occurring as the reaction proceeds from **A** to **C**, with the intent of comparing the model and enzymatic systems.

B. Results and analysis

I. Spectroscopy of intermediates

***Absorption spectra of* P^{DBED}, A, B, and C—**The UV/Vis absorption spectra of **P^{DBED}**, **A**, **B**, and **C** are shown in Figure 1. **P^{DBED}** exhibits a characteristic intense 28,500 cm^{-1} (350 nm, ε = 36,000 M^{-1} cm^{-1}) band associated with a side-on-peroxo π$_\sigma$ * – Cu(II) d$_x$2$_{-y}$2 charge transfer (CT) and a weaker band at ~20,000 cm^{-1} (500 nm, ε = 1,000 M^{-1} cm^{-1}) assigned to out-of-plane peroxo – Cu(II) CT.[11, 14, 34, 35] Addition of > 2 equivalents of phenolate at 153K maximizes the formation of intermediate **A** (Scheme 2), with markedly different absorption features from **P^{DBED}**. Three main features exist: a ~34,000 cm^{-1} band (295 nm, ε = 20,000 M^{-1} cm^{-1}), a ~23,900 cm^{-1} band (418 nm, ε = 18,000 M^{-1} cm^{-1}), and a less intense ~15,800 cm^{-1} band (630 nm, ε = 3,800 M^{-1} cm^{-1}). The intense ~34,000 cm^{-1} band exists in all spectra except **P^{DBED}** and is associated with excess phenolate in solution. At 153K, **A** converts within hours to intermediate **B**, with no strong (i.e. ε > 1000 M^{-1} cm^{-1}) absorption feature in the visible region. **C** results from the addition of sufficient equivalents of protons to neutralize the added phenolate to **B**. **C** is a purple complex with an absorption band at ~18,200 cm^{-1} (550 nm, ε = 3,000 M^{-1} cm^{-1}).

Intermediate A

Vibrational data: Resonance Raman (rR) data in the metal-ligand region of **A** along with ^{18}O isotope perturbations demonstrate clearly that **A** is a bis-μ-oxo dicopper(III) complex based on the presence of a 598 cm^{-1} peak which shifts by 25 cm^{-1} upon ^{18}O$_2$ substitution (Figure 2). These features and shifts are characteristic of the symmetric stretch of a bis-Cu(III) – bis-oxo type complex.[15] Additional isotope substitution experiments were made by

combining ^{16}O and ^{18}O substituted 2,4-di-*tert*-butylphenolate with $^{16}O_2$ and $^{18}O_2$, resulting in four possible isotopic combinations: $^{16}OPh^-/^{16}O_2$, $^{16}OPh^-/^{18}O_2$, $^{18}OPh^-/^{16}O_2$, and $^{18}OPh^-/^{18}O_2$. Six peaks are sensitive to both phenolate and O_2 isotopic substitution. Based on large $^{18}O_2$ isotope shifts, the vibrations at 657, 598, and 569 cm^{-1} are assigned as modes of the Cu_2O_2 core. Importantly, phenolate isotopic substitution perturbs the primary Cu_2O_2 core modes, verifying that phenolate is bonded to the bis-µ-oxo complex in an equatorial position of the Cu. Coupling from an axially bonded ligand would be insufficient to perturb the Cu_2O_2 core modes. In addition to the three Cu_2O_2 core modes, **A** has four resonance-enhanced modes at 548, 521, 494, and 395 cm^{-1}. Normally, Cu_2O_2 species show one Cu_2O_2 symmetric core stretch and one Cu-N stretch, not seven vibrational features, as observed.

Typical phenolate aromatic ring modes were observed at 1,280 and 1,598 cm^{-1} for **A** upon 650 nm excitation (Figure 3B). The modes are assigned in Table 1. The 1,280 cm^{-1} peak has a ^{16}–$^{18}O_2$ shift of 20 cm^{-1} (Figure 3, inset), allowing its assignment as a v_{C-O} vibration, further verifying the presence of bonded phenolate. Additional aromatic modes were observed at 1,080, 1,186, and 1,486 cm^{-1} with 413 nm excitation (Figure 3A).

The Cu-L and core Cu_2O_2 modes can provide insight into the number and coordination of bonded phenolate ligand(s). A symmetric D_{2h} $Cu_2O_2N_4$ core has one symmetry-allowed Cu-L mode that gains intensity, which is the totally symmetric Cu-N stretching mode. This behavior is observed in rR spectrum of the $[[(MeO-MePY_2)Cu]_2(O_2)]^{2+}$ bis-µ-oxo dicopper (III) complex, for example, where one v_{Cu-N} vibration is observed at ~530 cm^{-1}.[36] **A** exhibits four Cu-L modes (*vide supra*), all in the range of alkyl amine v_{Cu-N} modes (with phenolate O-Cu mixed in, based on isotope perturbations in Figure 2B). Expected equatorial vibrations for one and two phenolates bonded to the Cu_2O_2 core in either a *cis-* or *trans-* configuration are shown in Table 2 (top). In both bis-phenolate structures, only the symmetric stretches highlighted in Table 2 (top) are expected to gain significant rR intensity, resulting in one v_{Cu-N} vibration and one v_{Cu-OPh} stretch for each structure. For a mono-phenolate, the structure's molecular symmetry is decreased, and multiple v_{Cu-N} modes, which mix with v_{Cu-O} modes, would be observed in the rR spectra. The observation of four Cu-L modes indicates that only one phenolate is bonded equatorially. From ^{18}OPh, the 494 cm^{-1} band shows significant phenolate-Cu stretching character and virtually no $^{18}O_2$ dependence. The 548 cm^{-1} band is not sensitive to oxygen isotopic substitution and is assigned as the symmetric v_{Cu-N} of the two equatorial amines bonded to the Cu that is not ligated to phenolate. The 521 and 594 cm^{-1} bands are assigned as a combination of stretches of the copper center with a equatorial phenolate and diamine.

The v_{Cu-O} modes further confirm this assignment. As only symmetric modes are enhanced in the rR spectrum for a given structure, only two Cu_2O_2 core symmetric A_1 normal modes will be symmetry allowed for a *cis*-bis-phenolate structure with effective C_{2v} symmetry. Likewise, only two A_g modes would be symmetry allowed for a *trans*-bis-phenolate structure with effective C_{2h} symmetry. However, the single-phenolate structure, with C_s symmetry, could exhibit up to four enhanced v_{Cu-O} modes, three of which are experimentally observed, further confirming a single equatorially-bonded phenolate complex as the identity of **A**.

The expected core distortion (DFT-calculated structure of **A**, *vide infra*) for the equatorially-bonded phenolate is represented by a linear combination of the A_g, B_{2u}, and B_{3u} distortions in D_{2h} symmetry (Table 2). The most intense core distortion will be the A_1 mode (A_g in D_{2h}; A$'$ in C_s), which is assigned to the 598 cm^{-1} band. The other two v_{Cu-O} modes at 657 and 569 cm^{-1} are assigned as the C_s representations of the D_{2h} B_{2u} and B_{3u} modes, respectively.

rR profiles: Both the ~23,800 cm^{-1} and ~15,400 cm^{-1} absorbance bands of **A** were profiled in the Cu-L and intraligand regions of the rR spectrum with multiple excitation energies (Figure

4). The high energy absorption band is dominated by the 598 cm^{-1} A′ (in C$_s$ symmetry) core mode. The 657 cm^{-1} B$_{3u}$ ν_{Cu-O} mode and the Cu-L modes at 521 and 494 cm^{-1} also profile across the ~23,800 cm^{-1} band. This behavior is consistent with the assignment of the ~23,800 cm^{-1} band as an oxo-Cu(III) CT transition. Both the ν_{Cu-O} and Cu-L modes also profile weakly across the ~15,400 cm^{-1} band. From Figure 4 (bottom), the phenolate ring modes at 1,598 and 1,280 cm^{-1} (16–^{18}OPh$^-$ = 20 cm^{-1}) profile across the ~15,400 cm^{-1} absorption band, allowing assignment of this transition as a phenolate-to-Cu(III) CT transition. Alternatively, the other phenolate ring modes at 1,080, 1,186, and 1,486 cm^{-1} are resonance-enhanced in the higher energy band, but not the lower energy band. The two distinct sets of phenolate ring modes indicate that two distinct phenolate-to-Cu charge transfers exist, one at ~15,400 cm^{-1} and another overlapping the ~23,800 cm^{-1} oxo-to-Cu(III) CT band, with different excited state distortions.

The two highest energy occupied orbitals available in a phenolate for CT to the Cu are the π in-plane (π_{ip}) and π out-of-plane (π_{op}) orbitals, with the latter at higher energy, leading to a lower energy phenolate-Cu(III) CT transition. Charge transfer transitions from these two orbitals lead to different excited state distortions and thus enhance different ring modes. This was tested with DFT calculations in which an electron was selectively removed from either the π_{ip} or π_{op} phenolate orbital, and the geometry was optimized and compared to that of the ground state. The π_{op} CT distorts along the C$_1$-O, the *ortho*-C – *meta*-C, and the *meta*-C-H bonds, which enhances the 1,598 and 1,280 cm^{-1} vibrations, (Table 1) while the π_{ip} CT distorts along the C$_1$-O, C$_1$-*ortho*-C, *meta*-C – *para*-C, *ortho*-C-H, and *meta*-C-H bonds, which enhance the 1,486, 1,186, and 1,080 cm^{-1} vibrations. Phenolate vibrations expected to be enhanced by the excited state distortions associated with the π_{op} CT are present in the ~15,400 cm^{-1} absorption band, while the vibrational modes associated with the excited state distortion generated by the π_{ip} CT are enhanced in the ~23,800 cm^{-1} band. The rR profiling allows the low-energy transition to be assigned as a phenolate π_{op}-Cu CT, while the higher energy π_{ip}-Cu CT contributes intensity in the ~23,800 cm^{-1} region.

Further inspection of the rR profiles and enhancement patterns provides insight into the orientation of the phenolate ring with respect to the Cu$_2$O$_2$ core. Based on overlap of the phenolate donor orbitals with the Cu d$_{x^2-y^2}$ acceptor orbital, a dihedral orientation of 0° or 90° of the phenolate ring relative to the Cu$_2$O$_2$ core would produce CT intensity and associated resonance enhancement of vibrations associated with only the π_{ip} or π_{op} CT, respectively. The two distinct enhancement patterns observed in the rR profile of **A** in the intraligand region (Figure 4, bottom) require that the phenolate must be oriented at an intermediate angle. The vibrations associated with π_{op} phenolate-Cu CT transition (1,598 and 1,280 cm^{-1}, Table 1) are enhanced in the low energy region (~15,400 cm^{-1}) and the three vibrations enhanced by the π_{ip} phenolate-Cu CT transition are enhanced at higher energy (~23,800 cm^{-1}). Even though the higher energy absorption band has much more intensity than the lower energy band, the two vibrations associated with the low energy band are more resonantly enhanced relative to the three vibrations enhanced by the high energy band (Figure 4, bottom) as evidenced by their near-equal profile intensities despite the variation in ε of their associated absorption bands. Given that rR enhancement is proportional to the square of absorbance intensity and that the intensity of a CT transition is an indication of orbital overlap, more enhancement in the lower energy π_{op} phenolate-Cu CT transition indicates that the phenolate dihedral would favor π_{op} overlap. A phenolate orientation between 45° and 90° with respect to the Cu$_2$O$_2$ core is thus indicated by these resonance Raman profile data.

Geometry optimized structure and correlation to spectroscopy: The spectroscopically-derived model of **A** is supported by a DFT geometry-optimized structure in which the *tert*-Bu substituents of the phenolate are replaced by protons (Figure 5). The Cu-Cu distance of 2.83 Å and the O-O distance of 2.34 Å are indicative of a bis-μ-oxo dicopper(III) core. The plane

of the phenolate ring is tilted 74.7° with respect to the Cu_2O_2 core, in good agreement with the orientation indicated by the rR profile data presented above. The geometrical parameters of the Cu_2O_2 core in the DFT-derived model follow the vibrational distortion pattern presented at the bottom of Table 2. A characteristic bis-Cu(III)-bis-oxo core exhibits equivalent Cu-O bond lengths and Cu-O-Cu angles, but the DFT model of **A** is distorted in a manner consistent with the combination of the B_{2u} and B_{3u} modes of D_{2h} symmetry. The phenolate-bonded Cu has Cu-O_{distal} and Cu-$O_{proximal}$ bond lengths of 1.89 and 1.85 Å, respectively (labeled in Figure 5). Cu_B-O_{distal} and Cu_B-$O_{proximal}$ bond lengths of 1.81 and 1.80 Å, respectively. The Cu_A-$O_{proximal}$-Cu_B and Cu_A-O_{distal}-Cu_B bond angles are 101.4° and 99.5°, respectively. These geometric distortions lead to the rR intensity observed in the otherwise non-totally symmetric B_{2u} and B_{3u} normal modes.

Time-dependent DFT (TD-DFT) calculations of the absorption spectrum of **A** are compared to the experimental spectrum in Figure 6. The energies and oscillator strengths of 30 TD-DFT-predicted singlet charge transfer transitions of **A** are presented, six of which have oscillator strengths greater than 0.01 (see supporting information Figure SI.1 for depiction of the orbitals involved in these transitions). The lowest-energy transitions with non-zero oscillator strength at 11,400 and 11,500 cm^{-1} are predominantly phenolate π_{op} to Cu $d_{x^2-y^2}$ ligand to metal CT (LMCT) transitions (i.e. MO 159 → 160 α and β, and MO 159 → 161 α and β), with low oscillator strengths (~0.0027). A set of three moderately strong transitions (E (cm^{-1}), oscillator strength: 14,800, 0.0111; 15,900, 0.0218; 16,700, 0.0116) comprise an absorption band centered at ~15,800 cm^{-1}, assigned as mixed π_{ip} and π_{op} phenolate-Cu LMCT transitions, which is at-odds with the rR profile data since only the π_{op} phenolate-Cu CT transition is enhanced in the lowest energy region. Two intense transitions (18,800, 0.1059; 20,500, 0.0546) create an intense feature centered near 19,000 cm^{-1} in the simulated spectrum. The most intense of these features, at 18,800 cm^{-1}, has major contributions from the following transitions: MO 159 → 161 α and β π_{op} phenolate to Cu CT; MO 155 → 161 α and β π_{ip} phenolate to Cu CT; 151 → 161 α and β oxo to Cu CT. This significantly mixed transition should produce excited state distortions of the Cu-O_{oxo} and Cu-$O_{phenolate}$ vibrations (these are both enhanced in the high energy region of the rR profiles of **A**). The second strongest transition, at 20,500 cm^{-1}, has strong π_{ip} phenolate to Cu character (155 → 160 α and β; 156 → 161 α and β). This transition agrees with the rR enhancement of π_{ip} phenolate modes in the high energy absorption band. Finally, the moderately strong transition at 22,900 cm^{-1} (0.0255) has contributions from oxo to Cu excitations (151 → 161 α and β; 153 → 160 α and β; 154 → 160 α and β), which is present in this energy region, but with greater intensity. The presence of the large simulated band nearly 5,000 cm^{-1} below the intense experimentally-observed absorption band possibly stems from an underestimation of Cu-O bond covalency by the B3LYP hybrid-GGA functional or lack of a solvent field in the computational model, which can shift absorption bands by several thousand wavenumbers.[37–39]

DFT vibrational frequency calculations on a model of **A**, including $^{18}O_2$ and ^{18}OPh substituted isotopomers provide predicted vibrations and associated isotopic shifts (Table 2, middle). The core of **A**, with C_s symmetry was approximated with D_{2h} symmetry to correlate to the normal coordinate analysis (NCA) of Henson *et al.*[40] Four normal modes of the D_{2h} Cu_2O_2 core are shown in Table 2 (middle), along with NCA-predicted vibrations and isotopic shifts. Upon inspection of the non-scaled DFT-predicted vibrational modes of **A**, four vibrations were assigned as the B_{3u}, B_{1g}, A_g and B_{2u} normal modes of the D_{2h} core. The A_g mode, predicted at 601 cm^{-1} (exp. 598 cm^{-1}), exhibits calculated isotopic shifts with both ^{18}O dioxygen and phenolate as experimentally observed. The B_{3u} mode is predicted at 658 cm^{-1} (exp. 657 cm^{-1}), and the B_{2u} mode at 517 cm^{-1} (exp. 569 cm^{-1}). The B_{1g} mode is not observed in the rR spectrum, but is predicted at 650 cm^{-1} in the DFT calculation.

These frequency calculations also allow correlation to the Cu-L and intraligand vibrational modes in **A**. The frequencies, isotopic shifts, and associated atomic displacements are collected in Table 3. Based on observed isotopic shifts, three isotope-dependent Cu-L vibrations were calculated at 403, 458, and 515 cm^{-1}, corresponding to rR-observed vibrations at 395, 494, and 521 cm^{-1}, respectively, which were assigned above through rR profiling as mixed Cu$_2$O$_2$ core/Cu-N modes. The experimental rR trends of the isotopic shifts are reproduced in the calculated Cu-L vibrational modes. The 395 and 494 cm^{-1} vibrations, which contain Cu-phenolate stretching, are expected to show more isotopic dependence on ^{18}OPh substitution than on ^{18}O$_2$ labeling; this behavior is observed in both the rR experiments and in the vibrational frequencies of the computational model. Likewise, the aromatic ring modes are also computational reproduced (Table 3, bottom), showing only one isotope-dependent vibration at 1,280 cm^{-1}, indicative of the only phenolate normal mode that incorporates the C$_1$-O stretch. Experimentally, this mode shows no ^{18}O$_2$ dependence, but a -20 cm^{-1} shift upon ^{18}OPh$^-$ substitution. In the calculated model, a large ^{18}OPh dependence (-11 cm^{-1}) is predicted. The energies of the other four rR-observed aromatic ring modes are reproduced approximately in the DFT calculations within < 50 cm^{-1} and none are predicted or observed to exhibit isotope dependence.

Intermediate B—A decays via a first-order process at 153 K (t$_{1/2}$ = 20 min.) to **B** (Scheme 2) which has a nearly identical absorption spectrum as the reaction of **P^{DBED}** with 2,4-di-*tert*-butylphenolate at 193 K without the appearance of **A**, suggesting that the conversion of **A** to **B** is the rate-determining step in the overall reaction. **B** is an EPR silent species that exhibits no appreciable absorption feature in the visible region, precluding rR experiments. As **A** decays directly to **B**, an isoelectronic isomer is suggested, such as a bis-Cu(II)-μ$_2$-hydroxy dimer with an asymmetrically ligated catecholate as is obtained from the DFT calculations presented below (Figure 7). The lack of intense LMCT bands is consistent with other catecholate-dicopper(II) complexes,[41, 42] which exhibit only weak bands (ε < 1,000 M^{-1} cm^{-1}) in the visible region.

TD-DFT calculations, which qualitatively correlate to the experimentally-observed CT bands in **A** (*vide supra*) and **C** (*vide infra*) do not predict any intense visible transition for this model of **B**. This reflects the lack of orbital overlap between the catecholate and Cu(II) ions (see the MO depictions of **B** in Figure SI.2). The experimental absorption spectrum of **B** (from Figure 1) is overlaid with the TD-DFT predicted transitions and simulated absorption spectrum in Figure SI.3, and the orbitals involved in the TD-DFT-predicted transitions are given in Figure SI.2. There are two transitions with non-zero oscillator strength in the near-IR region predicted by the calculations. The transition at 9,100 cm^{-1} (oscillator strength = 0.0336; 168 → 169 α and β) is attributed to symmetric catecholate π$_{op}$ to Cu CT. A second transition at 12,800 cm^{-1} (oscillator strength = 0.0131; 167 → 169 α) is due to antisymmetric catecholate π$_{ip}$ to Cu CT. No other predicted transition has an oscillator strength greater than 0.01.

Intermediate C

Vibrational data: The addition of an equimolar amount of protons to the phenolate added to create **A** converts **B** to **C**, a purple species. The proton addition reproduces the stoichiometry of the tyrosinase mechanism. The geometric and electronic structures of **C** were evaluated in a manner similar to **A**, using rR vibrations, profiles, and DFT calculations. The high-energy intraligand region of the rR spectra of **C**, collected using 530 nm (~18,000 cm^{-1}) excitation, including isotopic shifts upon formation with ^{18}OPh and ^{18}O$_2$ (Figure 8). Two vibrations are isotopically sensitive at 1,375 and 1,435 cm^{-1}, with each band more tightly coupled to ^{18}OPh substitution than to ^{18}O$_2$ substitution. These features are consistent with C-O/ring mixed modes observed for metal-bonded semiquinone species[43, 44] and allow assignment of **C** as a Cu(II)-semiquinone complex. The low-energy region of the rR spectrum (Figure 9), reveals six vibrations with isotope dependence: 436, 508, 557, 577, 676, and 748 cm^{-1}. Each vibration

couples with ^{18}O labeling of both phenolate and dioxygen except the 436 cm^{-1} vibration which does not shift upon ^{18}O$_2$ substitution. *The strong coupling between the two isotope perturbations indicates that the oxygen atom inserted into the phenolate to form the semiquinone product derives from O$_2$, and thus from the oxo bridge of **A**.*

rR profiles: The ν_{C-O} and dominant Cu-L modes of **C** were profiled across the ~18,000 cm^{-1} absorption band. The ν_{C-O} modes are enhanced similarly across this broad feature (Figure 10, top). The non-Gaussian bandshape of the profile indicates the presence of at least two electronic transitions. The Cu-L modes also clearly show evidence for two transitions, one at ~19,000 cm^{-1} and another at ~16,500 cm^{-1}, as two distinct Cu-L enhancement patterns are observed (Figure 10, bottom). The 557 and 508 cm^{-1} vibrations, which have nearly equal phenolate and dioxygen isotope dependence, are enhanced more strongly in the ~19,000 cm^{-1} region while the 577 cm^{-1} mode is enhanced more strongly near ~16,500 cm^{-1}.

Geometry optimized structure and correlation to spectroscopy: The reaction coordinate-predicted structure of **C** (*vide infra*) is given in Figure 11. In order to elucidate the electronic structure of **C**, DFT calculations were performed on a model of **C** with a semiquinone (SQ) bound to Cu(II). The DBED ligand is bonded to Cu(II) with the *tert*-Bu groups on the amines oriented *trans*- to one another. The plane of the semiquinone ring is rotated 32° relative to the Cu-N plane. Inspection of the molecular orbitals of this structure (Figure 12) shows a Cu(II)-based α hole and a semiquinone-based β hole (92α and 92 β), corresponding to antiferromagnetic (a.f.) coupling between the metal ion and the semiquinone. The semiquinone species is further exemplified by the β LUMO (92β) corresponding to the α HOMO (91α). The 32° dihedral angle, φ (N-Cu-O-C), observed in the geometry-optimized structure is sufficiently large to allow overlap between the orbitals of Cu and the ring, producing the a.f. ground state with the broken-symmetry singlet energy 1.1 kcal/mol lower in energy than the triplet state.

DFT frequency calculations yield two ν_{C-O} normal modes, two ν_{Cu-O} modes, and two mixed modes, as shown in Table 4 along with experimental and calculated isotope shifts. The four experimentally observed Cu-L vibrations at 748, 577, 557, and 508 cm^{-1} are assigned from the calculations as two ν_{Cu-O} and two chelate/Cu-N mixed modes, respectively. Chelate modes involve in-plane bending of the O-Cu-O bond angle. The 748 and 577 cm^{-1} modes are nearly pure Cu-O bond stretching modes with additional mixing of ring motion, while the 557 and 508 cm^{-1} vibrations are mixed chelate and Cu-N in character, as shown in the normal mode displacements in Table 4. One chelate mode is present generally for a five-membered ring formed from a chelating aromatic ligand bonded to a metal.[45] The two modes correspond to the two five-membered chelate rings in **C**: one incorporating Cu and the semiquinone, and the other the Cu and the diamine ligand. The 508 and 557 cm^{-1} modes (calculated at 500 and 521 cm^{-1}, respectively) are symmetric due to the D$_{2d}$ distortion of the complex from a square planar geometry, allowing for rR enhancement. This is reflected in the intensity pattern seen in the rR spectrum (Figure 9) as the 557 cm^{-1} mode is much more intense than the 508 cm^{-1} mode. The 508 cm^{-1} mode is assigned as a chelate mode mixed with ν_{Cu-N} and out-of-plane ring bending, and the 557 cm^{-1} mode is the main chelate mode, incorporating a large O-Cu-O angle bending motion that mixes with Cu-N bond stretching. rR isotope data reveal that both O$_2$ and phenolate substitution significantly affect these mixed chelate modes, as calculated. Two ν_{Cu-O} modes are observed at 577 and 748 cm^{-1} (calculated at 607 and 758 cm^{-1}, respectively) and both mix with semiquinone modes. The 577 cm^{-1} peak derives most of its intensity from ν_{Cu-O}, with mixing of a symmetric ring breathing mode. The 758 cm^{-1} mode couples with ν_{C-C} of the semiquinone. Metal-oxygen stretches are known to mix with such intraligand C-C stretches.[44] The two modes at the bottom of Table 4 are different ring stretching modes that couple with C-O bond stretches. The observed vibrations at 1,435 and 1,375 cm^{-1}, calculated at 1,487 and 1,393 cm^{-1}, respectively, are consistent with C-O stretching modes in other metal-

semiquinone complexes.[43] The C-C stretches involved in each of the modes are shown in Table 4.

The magnitudes of the experimental phenolate and O_2 isotope shifts are greater than the calculated values (i.e. the experimental modes are less mixed), and the calculations show equal isotope dependence on both oxygen atoms whereas experimentally the two oxygens contribute unequally in each of the five modes. The calculated structure of **C** shows that the two Cu-O bonds have the same length and the two C-O bonds are also equal, which results in the equivalent calculated isotope effects. The unequal isotope shifts in the rR spectra of **C** (see Table 4), indicate that the experimental structure of **C** has inequivalent Cu-O and C-O bond lengths. The differences between experimental and calculated isotope dependencies may stem from the use of an unsubstituted ring in the computational model while the experimental structure is a 2,4-di-*tert*-butylsemiquinone, which would impose steric effects on the real system not present in the computational model.

Correlation of the band assignments to the rR profile data further characterizes the nature of the associated electronic excited states of **C**. The two modes assigned as having mixed chelate/ Cu-N character are more enhanced in the ~19,000 cm^{-1} region than in the ~16,500 cm^{-1} region (557 and 508 cm^{-1}, Figure 10, bottom), thus these modes distort more in the excited state associated with the higher energy electronic transition. The 577 cm^{-1} ν_{Cu-O} exhibits the opposite behavior, with greater ν_{Cu-O} distortion associated with the lower energy electronic transition. The near-equivalent intensity enhancement of the two ν_{C-O} modes (1,375 and 1,435 cm^{-1}; Figure 10, top) indicates that significant excited state distortion in the C-O bonds occurs in both electronic transitions.

TD-DFT calculations help evaluate the nature of the electronic transitions in **C** at ~19,000 and ~16,500 cm^{-1}. An overlay of the experimental and calculated absorption spectrum along with the corresponding TD-DFT-predicted transitions (Figure 13) show reasonable agreement. The simulated spectrum is dominated by three moderately strong electronic transitions in the low energy visible and NIR regions. The molecular orbitals involved in these electronic transitions are included in Figure 12. The first low-energy transition with non-zero oscillator strength is at 9,200 cm^{-1} (Figure 13) and is strongly associated with semiquinone π_{op} to Cu LMCT (oscillator strength = 0.0183; 91 → 92 α). The next intense transition at 16,600 cm^{-1}, has many contributions: 88 → 92 α, antisymmetric π_{ip} SQ to Cu LMCT; 80 → 92α, π_{ip} antisymmetric SQ to Cu LMCT; 91 → 92 α, π_{op} SQ to Cu CT; 90 → 92β, π_{ip} symmetric SQ to π_{op} SQ intraligand transition with MLCT character; and 85 → 92 α, π_{op} SQ to Cu LMCT. The dominant SQ to Cu CT leads to an excited state distortion mostly along the Cu-O bonds, which resonance-enhances in the Cu-O stretch in the ~16,600 cm^{-1} region (Figure 10). These transitions also agree with the mixing of modes observed in the DFT frequency calculations in that the Cu-O stretches are mixed with both in-plane and out-of-plane semiquinone ring motion. The third strong predicted transition at 18,600 cm^{-1} (Figure 13) with an oscillator strength of 0.0205, is comprised of two transitions: 90 → 92 β, π_{ip} symmetric SQ to π_{op} SQ intraligand transition with MLCT character; 88 → 92 β, π_{ip} antisymmetric SQ to π_{op} SQ with some MLCT character. This transition involves mainly intraligand excited state distortion which leads to resonance enhancement of the chelate modes in the ~18,600 cm^{-1} region, as observed in the rR profiles (Figure 10, bottom). The 90 → 92β excitation results in moderate excited state distortion and resonance enhancement of the SQ oxygen σ-bonding to π_{op}-bonding. The 88 → 92β excitation results in significant excited state distortion and resonance enhancement of the SQ oxygen σ* to π_{op}-bonding. The 90 → 92β excitation, which contributes to the 16,600 and 18,600 cm^{-1} TD-DFT transitions, also contains MLCT character, as evidenced by the MO coefficients of Cu(II) mostly in the donor orbital. 90β contains 24% Cu(II), while 92β, the β LUMO, contains less than 1% Cu(II) character and 97% SQ character. Likewise, the predominantly intraligand 88 → 92β transition exhibits 21% Cu(II) in the donor orbital and 1% Cu and in the acceptor

orbital and contributes to the high energy TD-DFT-predicted transition. The MLCT character of these excitations mixed with the intraligand chelate of the high energy absorption band results in enhancement of Cu-O stretches in that region as well.

II. Computational studies of the reaction coordinate

Geometric and Electronic Structure of A—The rR data of **A** are most consistent with a mono-phenolate bis-μ-oxo dicopper(III) complex, and the calculated electronic and geometric structures of **A** correlate to the observed electronic absorption features including the oxo-Cu LMCT at ~24,000 cm^{-1} and the phenolate-Cu(III) LMCT at ~16,000 cm^{-1}. The computational model of **A** has an unsubstituted phenolate bonded to the bis-oxo core supported by the DBED ligand (Figure 5). The distance between the $O_{proximal}$ bridge and the nearest *ortho*-carbon atom of the phenolate was constrained at 2.80 Å during geometry optimization; Table 5 gives some parameters of the optimized structure. Within the Cu_2O_2 core, Cu-O bond lengths vary between 1.80 and 1.89 Å, as given previously. The core distorts from a symmetric bis-μ-oxo geometry as shown at the bottom of Table 2. The Cu-Cu and O-O distances, at 2.82 Å and 2.35 Å, respectively, are reminiscent of a bis-Cu(III)-bis-oxo core. Cu_B is bonded to DBED with Cu-N bond lengths of 2.01 and 2.04 Å, while the phenolate-bonded Cu_A exhibits unequal Cu-N bond lengths to its diamine ligand. The Cu_A-N bond distance in the equatorial plane of the Cu is 2.04 Å, and the other Cu_A-N bond is in an axial position at 2.40 Å. The phenolate oxygen to Cu_A distance is 1.88 Å.

Molecular orbitals of **A** (Figure 14) clearly show the presence of a hole on each Cu center (α and β LUMO and LUMO+1) verifying a Cu(III) designation. The spin densities are also approximately zero, in line with a d^8 Cu(III) center. The occupied orbitals on the aromatic ring confirmed it as a phenolate. By examination of the two lowest unoccupied α and β orbitals, the electronic structure of the bis-oxo Cu_2O_2 core has oxo σ^* character mixed into the LUMO and the oxo π^*_σ character mixed into the LUMO+1. Of particular interest are the spatial orientations and compositions of the HOMO and LUMO (same in α and β). The HOMO is a pure phenolate symmetric π^*_{op} orbital, while the LUMO is Cu_2O_2 core-based anti-bonding orbital with contributions from both Cu $d_{x^2-y^2}$ and oxo σ^* orbitals. If the plane of the aromatic ring is tilted to 75° with respect to the plane of the Cu_2O_2 core, as computationally predicted, the π^*_{op} occupied phenolate orbital (HOMO) is well positioned for electrophilic attack on the neighboring σ^* orbital of the $O_{proximal}$ (LUMO) as seen in Figure 14.[15]

Reaction coordinate of C-O bond formation—A seven point potential energy surface (PES) tracing the contraction of the C-O distance in the model of **A** from 2.80 to 1.30 Å is presented in Figure 15 (right to left). The highest-energy state along the coordinate is identified at a C-O distance of 2.10 Å. Further constriction of the C-O distance results in appreciable lowering of the electronic energy of the system. The calculated energy barrier of 4.5 kcal/mol is within DFT accuracy of the experimental activation energy of 7.3 kcal/mol.[46] The difference may also be attributed to solvent effects or the truncation of the computational model compared to the experimental system since our model contains an unsubstituted phenolate ligand.

$$\frac{k_D}{k_H} = e^{\left\{-\frac{hc}{2kT}\left(\sum(\bar{v}'_D - \bar{v}'_H) - \sum(\bar{v}_D - \bar{v}_H)\right)\right\}}$$

(1)

The highest-energy state shows distortion of the *ortho*-C from a planar sp^2-like carbon to a tetrahedral-like sp^3 carbon, and a modest shortening of the *ortho*-C-H bond, corresponding to a slight increase in the stretching frequency of the bond, from 3,185 cm^{-1} in **A** to 3,205 cm^{-1}. These data directly correlate to the experimentally-observed inverse secondary KIE of the reaction. Application of the Streitweiser approximation[47] (Equation 1) to the *ortho*-C-H

bond in the highest energy structure predicts an inverse 2° KIE of 0.95 (± 0.18), which is similar to the observed inverse 2° KIE of 0.83 (± 0.09). Since the C-H bond is strongest at the highest-energy calculated state, as in the experimental system, the calculations show that the rate-limiting step of the reaction is that of the distortion of the phenolate ring.

In this simulation, no provision for the *ortho*-C-H bond cleavage is allowed; therefore the *ortho*-C tends to a tetrahedral geometry as the C-O distance is shortened. Several diagnostics were calculated to evaluate whether the C-O bond completely forms at short C-O distances and with the *ortho*-C-H bond still intact. In the next section, an accessible proton acceptor is simulated in the reaction coordinate, and it is shown that C-H bond dissociation is a necessary precursor to C-O bond formation.

The Mayer's Bond Order (MBO) for the C-O interaction increases with decreasing distance between the atomic centers (Table 6), and in the structure with a 2.10 Å C-O distance indicates that the C-O bond is only partially formed. The MBO of greater than 1.0 for short C-O distances is misleading, as the MBO of a normal catecholate C-O bond is ~1.5. Furthermore, natural bonding orbital (NBO) overlap and the Wiberg Bond Index (Table SI.1) for the computational model are lower than for normal catecholate. Taken together, these data suggest that the C-O bond is not fully formed while the *ortho*-C-H bond exists. As the C-O distance decreases, the *ortho*-H becomes more proton-like, indicated by the increase in its Mulliken charge (Table 6).

Investigation of the MOs along the reaction coordinate (Figure SI.4) provides valuable insight into the electronic structural changes occurring during this process. Inspection of the MOs and a comparison of the broken-symmetry and restricted singlet energies of the 2.80 Å (Intermediate **A**) and 2.30 Å structures reveals that the complex exists as a phenolate bonded to a bis-μ-oxo dicopper(III) core at these points. Structures with *ortho*-C-O$_{proximal}$ distances of 2.30 to 2.00 Å, including the TS of the reaction, exhibit several electronic changes relative to the starting complex. First, as the *ortho*-C distorts from a planar configuration, the ring-based HOMO resembles that of a distorted phenolate, and the bis-oxo character of the unoccupied orbitals becomes more obscure, i.e. the π^*_σ and σ^* oxo character lessens and the Cu centers exhibit polarization in the α and β LUMO+1, 2.10 Å structure. As the C-O distance is reduced below 2.0 Å, the MO coefficients of the aromatic ligand and the two Cu ions reveal increasing contributions from the aromatic ring into both the α and β LUMO (i.e. two holes form on the ring in the 1.50 Å structures: MO 160α and 780β). The coefficients of the phenolate-based α and β HOMO decrease (57% α to 34% α and 60% β to 27% β proceeding from 2.10 Å to 1.90 Å C-O). This indicates that soon after the transition state, two electrons simultaneously transfer from the distorted phenolate to the two Cu(III) ions, reducing each to Cu(II) and creating a doubly-oxidized distorted phenolate ligand. The presence of two a.f.-coupled Cu(II) ions is confirmed by the presence of one hole on each Cu ion (Figure SI.4: 1.90 Å structure, 161α and 780β; 1.50 Å structure, 161α and 779β). In the 1.30 Å structure, the HOMO of the aromatic ring has unequal contributions from the two C-O interactions, resulting in a distortion of the symmetric π_{op} ring-based orbital (Figure SI.4, 1.30 Å C-O, HOMO α and β). This can be visually confirmed by examining the orientation of the O$_{phenolate}$ and O$_{proximal}$ orbitals relative to the occupied π_{op} catecholate orbital. Despite the fact that this structure has a constrained C-O distance of 1.30 Å (shorter than the typical catecholate C-O bond length of ~1.4 Å), the MOs indicate that the C-O bond is not fully formed.

Removing the *ortho*-H as a proton in a second simulation results in the formation of a full C-O bond, confirmed by molecular orbital and NBO analyses (Table SI.1). To illustrate the effect of the *ortho*-proton on C-O bond formation, the MO diagrams of two 1.50 Å structures are shown in Figure 16; one with an intact *ortho*-C-H bond (top) and one with a cleaved *ortho*-C-H bond (bottom). The nature of the ring-based α and β HOMO and HOMO-1 of the structure with the cleaved *ortho*-C-H bond are more catecholate-like and the α and β LUMO show the

a.f.-coupling of the Cu(II) ions (Figure 16, bottom). The a.f. coupling can also be seen in the model with the intact *ortho*-C-H bond, but the HOMO and HOMO-1 are not catecholate-like and there are two holes on the ring in the αLUMO and βLUMO+1 (Figure 16, top). This analysis reveals that the formation of the catecholate species is facilitated greatly by the cleavage of the *ortho*-C-H bond. After C-H bond cleavage, the C-O bond forms fully as two electrons from $O_{proximal}$ fill the two holes on the doubly oxidized distorted phenolate. Notice that the α and β HOMO of the *ortho*-C-H structure (top) are not ring-based, but when the *ortho*-proton is gone, the same HOMOs are predominantly catecholate-like in nature. MOs 160α and 780β in Figure 16 (top) show the two holes on the oxidized phenolate. These two holes are filled by electrons from $O_{proximal}$ upon C-O bond formation at the bottom of Figure 16.

Experimentally, heterolytic C-H bond cleavage requires a driving force, and the effect of a proton acceptor is evaluated in the next section. Also in the next section, the electronic transfers that allow catecholate formation are examined and the same catecholate-dicopper(II) species is generated after H^+ transfer from *ortho*-C-H (through an intermediary base) to the O_{distal} of the core.

Two-dimensional PES of C-O bond formation and C-H cleavage: dependence on the H^+ acceptor—A logical destination of the *ortho*-H^+ is the O_{distal} of the Cu_2O_2 core. Yet, the > 4.0 Å distance between the *ortho*-H and the O_{distal}, combined with the projection of the *ortho*-C-H bond vector will not allow a direct proton transfer. The large steric demands of the six *tert*-butyl substituents in the bridged copper dimers dramatically restrict the rotational rearrangement of the aromatic ligand to facilitate this proton transfer. Representing the atoms with van derWaals radii further illustrates this point (Figure SI.5).

ortho-C-H bond cleavage is necessary for full C-O bond formation, and direct proton transfer to the O_{distal} is unlikely. An exogenous base near the *ortho*-H site would facilitate C-H bond cleavage and eventual protonation of O_{distal}. Methylamine was modeled within the seven structures from the initial reaction coordinate with the lone pair pointing toward the *ortho*-H, along the C-H vector at a fixed distance of 3.10 Å. For each of these seven structures, the C-H distance was fixed at three different lengths with proton movement along the C-$N_{methylamine}$ vector.

The two-dimensional plot of the electronic energy of the system as a function of both C-O and C-H distance is presented in Figure 17. From the back left portion of the surface with a C-O distance of 2.80 Å and a C-H distance of 1.08 Å (**A**), the lowest-energy path resembles that of the base-free reaction coordinate (Figure 15), showing a TS near a C-O distance of 2.10 Å that exhibits a tetrahedral distortion of the *ortho*-C and indicates that ring distortion is the rate-limiting step. With the C-O distance sufficiently reduced (near 1.40 Å), proton transfer to the nearby methylamine is energetically favorable, and the system arrives at the lowest-energy region of the plot in the front right with a short C-O distance and a long C-H distance relative to the starting point.

As with the one-dimensional reaction coordinate (Figure 15), MBO and MO analyses of the structures calculated on the PES of the 2-D reaction coordinate were performed, and the MO are shown in Figure SI.6. The system originates as a phenolate bonded to the bis-μ-oxo dicopper (III) core (**A**), followed by reduction of the two Cu(III) ions to two Cu(II) ions by oxidation of the phenolate as evidenced by the two ring-based holes and the a.f.-character of the Cu(II) ions in the unoccupied orbitals. The addition of the methylamine proton acceptor in this simulation allows for late-stage proton transfer. Upon proton transfer, the ring is allowed to regain planarity and is reduced simultaneously by two electrons from $O_{proximal}$ as the C-O bond forms. The MBO of the C-O pair after proton transfer has a value of approximately 1.5 (Table 7)

which is higher than the 1.1 MBO calculated earlier for the base-free system in which there in no proton transfer.

Inspection of the unoccupied MO of $O_{proximal}$ in Figure SI.7 provides further evidence of catecholate formation. The C-O bond does not form fully until electrons are transferred from $O_{proximal}$ to the ring. Therefore, C-O bond formation results in a marked increase in the $O_{proximal}$ coefficient of an unoccupied molecular orbital. The unoccupied ring in-plane antibonding orbital is shown in Figure SI.7 along with the MO coefficients of both the ring and $O_{proximal}$. For the most part, the major contribution to these unoccupied orbitals is the ring, while $O_{proximal}$ character is always near 0% regardless of C-O distance as long as the *ortho*-C-H bond remains intact. At an *ortho*-C-O distance of 1.30 Å, as the proton is transferred to methylamine, the $O_{proximal}$ character in these same orbitals increases from 4% to 12% to 17% at C-H distances of 1.15 Å, 1.58 Å, and 2.08 Å, respectively, indicating the formation of two holes on the O (read down the Figure). These data confirm the formation of an asymmetrically-bridged catecholate bound to two a.f.-coupled Cu(II) ions.

A significant barrier to proton transfer exists for all C-O distances greater than 1.40 Å (Figure 17). To gauge the effects of the choice of exogenous base and heavy-atom distance between the *o*-C and the proton acceptor, an acetate ion was modeled in place of methylamine to provide a stronger base, and the *o*-C-$O_{acetate}$ distance was restrained to 3.10 Å (as with the *ortho*-C-$N_{methylamine}$) and 2.40 Å in separate simulations.

Using a *ortho*-C-$O_{acetate}$ distance of 3.10 Å, the PES shown in Figure SI.6 is generated. As expected, the proton transfer barrier is lower in this simulation since acetate is a stronger base than methylamine in vacuum. Furthermore, the energies of the structures on the right hand side of the surface (those where the proton has already been transferred to the acetate) are lower than those structures on the left hand side of the surface where the *ortho*-C-H bond is intact, which is indicative of the relative stability of the CH_3COOH structure over the protonated methylamine. However, the proton transfer barrier is still too high to be accessible to the reaction at *ortho*-C-proximal O distances longer than about 1.70 Å. Thus, the TS of the reaction is still near a C-O distance of 2.10 Å, meaning that even in the presence of the stronger proton acceptor, the rate limiting step is still ring distortion.

Constraining the *ortho*-C-$O_{acetate}$ distance to 2.40 Å, yields the 2-D PES given in Figure SI.7. The TS still exists near a C-O distance of 2.10 Å, and MO analysis shows that two holes still form on the aromatic ligand. It is evident by these data that the use of a stronger proton acceptor at close proximity does not lead to a remarkably different reaction coordinate than the previous simulations.

Effects of protonating the distal O—Whereas $O_{proximal}$ of the Cu_2O_2 core is inserted into the aromatic ring via the EAS mechanism, O_{distal} is not directly involved. However, the protonation state of O_{distal} plays a role in product formation after the C-O bond has formed. To investigate the effects of the protonation state of O_{distal} on product formation, the structure from the bottom right corner of the PES in Figure 17, in which the *ortho*-C-H proton has transferred to the methylamine, was modified by placing this proton on O_{distal}. In essence, this treats methylamine as a proton transfer catalyst. Figure 18 displays two isoatomic species generated after C-H bond scission, one with the protonated methylamine (left) and the other with a OH_{distal}. The species with OH_{distal} is ~25 kcal/mol lower in energy than the protonated methylamine structure, showing that proton transfer via an exogenous base is energetically favorable. Using this model, in which no protons have been added to the reaction, the electronic structure of the Cu_2O_2 core and of the aromatic ring is independent of the protonation state of O_{distal}, and both species are identified as asymmetrically-bound catecholate a.f.-coupled dicopper(II) complexes.

Without adding a proton to the system, the lowest energy species is that of an a.f.-coupled catecholate – dicopper(II) with a bridging OH group. Addition of one proton into the simulation at the distal OH position, the system spontaneously dissociates into two mononuclear components (Figure 18, right). The Cu not ligated to the aromatic ligand is reduced to Cu(I), while the other Cu remains oxidized and bonded to a semiquinone in a bidentate fashion. The dissociation of the dimer and formation of **C** allows the DBED ligand on the semiquinone-bonded Cu to return to equivalent Cu-N bond lengths of 2.02 Å. The mononuclear Cu(II) component of the computational system after addition of one proton is a proposed a.f.-coupled Cu(II)-semiquinone and exhibits all of the geometric and electronic structure features consistent with experimental data presented above.

C. Discussion

The hrdoxylation of phenolate by $\mathbf{P^{DBED}}$ has been evaluated spectroscopically and computationally, and the mechanism derived from these data is presented in Scheme 3. Axially binding of an exogenous phenolate to $\mathbf{P^{DBED}}$, followed by a rapid rearrangement of the side-on peroxy core to a bis-Cu(III)-bis-oxide core and an equatorial positioning of phenolate yields **A**. rR data clearly identifies **A** as a mono-phenolate ligated to a single copper center of a bis-Cu(III)-bis-oxide core. The electronic absorption spectrum of **A** possesses two intense bands in the visible region, a high energy band corresponding to oxo to Cu CT in the Cu_2O_2 core and a low energy transition indicating phenolate to Cu(III) LMCT. These band assignments are supported by rR profile experiments and (to some extent) TD-DFT calculations. rR profile experiments indicate that the plane of the phenolate ring is oriented between 45° and 90° relative to the plane of the Cu_2O_2 core, again supported by the DFT-calculated model of **A**. This orientation also aligns the phenolate-bonded HOMO and the Cu_2O_2-based LUMO (Figure 14) in a manner as to facilitate electrophilic attack by the proximal O atom on the *ortho*-carbon of the phenolate.

The subsequent *ortho*-hydroxylation of the ring is accomplished via electrophilic aromatic substitution. This mechanism is supported by the experimentally observed inverse 2° KIE of the *ortho*-C-H bond, indicating a hybridization change at the carbon from sp^2 to sp^3 and strengthening of the C-H bond at the TS (Scheme 3). Calculations correlate to experiments, indicating phenolate ring distortion as the rate-limiting step of the reaction leading to **B** from **A**. Coincident with ring distortion is the reduction of the two Cu(III) ions by CT from the aromatic ring. The phenolate-bonded Cu is reduced through the Cu-phenolate bond and the other Cu is reduced through the partially-formed *ortho*-C–$O_{proximal}$ bond. These electronic transitions create a doubly-oxidized phenolate bound to two antiferromagnetically-coupled Cu(II) ions. Partial C-O bond formation and reduction of the two Cu(III) ions assuage the energetically unfavorable ring distortion at the TS. The C-O bond does not fully form until heterolytic cleavage of the *ortho*-C-H bond and proton transfer to a proposed exogenous base.

Once the C-O distance is sufficiently short, proton transfer to the exogenous base is energetically favorable and a catecholate-dicopper(II) complex is formed. Proton transfer to O_{distal} via an exogenous base produces the lowest energy structure for this system. **B** exhibits no intense absorption feature in the visible region. Based on calculations and spectroscopy, **B** is proposed to be an asymmetrically-bonded catecholate-dicopper(II) species with a distal hydroxyl-bridge, which is a.f.-coupled.

Addition of one equivalent of proton to **B** produces **C**. rR isotope experiments on **C** show that one oxygen atom from O_2 is inserted into the ring. Addition of one proton to the hydroxy-bridge in **B** results in the dissociation of the dimer into two components: a Cu(I)-diamine-OH_2 monomer and a Cu(II)-semiquinone proposed to be a.f.-coupled.[48] The formation of **C** is driven by the double protonation of the distal O atom once the C-O bond has been formed.

The DFT-optimized structure of **C** reveals significant D_{2d} distortion of the four-coordinate Cu (II) that presumably leads to magnetic orbital overlap and an antiferromegnetic spin state for the system.

Relationship to the tyrosinase mechanism

With respect to the proposed tyrosinase mechanism, several parallels can be drawn between the enzymatic function and the reaction detailed in this study, particularly regarding changes in the electronic structure and protonation state of the biomimetic complex after the transition state. Prior to the TS, the model system and oxyTy may differ significantly. In particular, Karlin and coworkers have side-on-peroxo complexes that intramolecularly hydroxylate an aromatic C-H position.[17, 24, 49–51] If Ty shares a similar mechanism, an enzymatic analogue of **A** would not be present in the protein reaction cycle since Cu would not achieve the 3+ oxidation state. Extensive spectroscopic studies of oxyTy confirm the presence of a **P** species, but not **O**. If the **P**^{DBED} hydroxylation reactivity were only examined at 193 K rather than at 153 K, the only spectroscopically observed Cu_2O_2 species would also be a side-on peroxy. The issue of whether phenolate binding to oxyTy drives the formation of **O** remains an intriguing question. More similarities can be drawn between the **P**^{DBED} system and the enzyme at the TS and beyond. The similar Hammett parameter for the oxyTy and **P**^{DBED} supports the assertion that Ty proceeds through a TS in which aromatic ligand distortion is the rate-limiting step. Recently, altered hemocyanin which hydroxylates monophenolic substrates.[52, 53] was shown to exhibit an inverse 2° KIE of 0.9, which also agrees with experimental and computational data on **P**^{DBED}.

Model reactivity after the TS can also be expanded to the enzymatic system. In the model system, the TS structure proceeds to **B** upon dissociation of the *ortho*-C-H bond. The asymmetric binding motif of the catecholate in **B** is a slight variation of the mechanism shown in Scheme 1.[1, 9] This deprotonation could be accomplished in Ty by proton transfer to solvent since the active site in Ty is solvent-exposed, or to a nearby flexible His residue that was identified in the crystal structure of Ty.[54] The formation of **C** in the model system, corresponding to the formation of a dicopper(I)-quinone in Ty, is achieved upon the further protonation of the distal OH bridge of **B**. In the enzyme, this proton could also be provided by solvent, or via a chain of charged residues that reach from near the distal O of the active site through the protein to its far surface.[55] The formation of the Cu(II)-semiquinone in the model system is tied clearly to DBED ligation since the enzymatic system produces the quinone and two fully-reduced Cu ions. It is also interesting to note that the direct production of a quinone along with reduction of the Cu(II) ions to Cu(I) ions by the proximal oxide without proceeding through a catecholate intermediate is not supported by our results.

D. Materials and Methods

Synthetic

Synthetic methods are the same as previously reported.[16] All solvents and reagents were obtained from commercial sources and used as received unless noted otherwise. THF, 2-methyltetrahydrofuran (MeTHF), and toluene (Aldrich) were distilled from sodium/benzophenone. CH_2Cl_2 was stirred over H_2SO_4, washed with aqueous KOH followed by deionized water, and finally distilled from P_2O_5 in the absence of light. Acetone was refluxed (5 h) with anhydrous K_2CO_3 and distilled. All solvents were stored under a N_2 atmosphere. $[Cu(MeCN)_4](X)$ (X = $CF_3SO_3^-$, $CH_3SO_3^-$, SbF_6^-, BF_4^-) complexes were synthesized by a variation of literature methods.[56] Preparation and manipulation of Cu(I) complexes were carried out in a N_2 drybox (Braun) with O_2 concentration <1.0 ppm. N,N′-di-*tert*-butyl-ethylenediamine (DBED) was purchased from Aldrich, distilled *in vacuo* from CaH_2, and stored under N_2. The lithium or sodium salts of 2,4-di-*tert*-butylphenol were prepared

according to a reported procedure.[57] Low-temperature UV-Vis spectra were collected with a Polytec PI X-DAP-06 diode array spectrophotometer (190–820 nm) or a Cary 50 spectrophotometer (190–1100 nm) with a custom-designed immersible fiber-optic quartz probe with variable path length (1 and 10 mm; Hellma, Inc.). Constant temperatures were maintained either by a cooling bath (Kinetic Systems, New York) or a dry ice/solvent baths. The solution temperatures were monitored directly by insertion of an OMEGA temperature probe. Solution ^{1}H NMR and ^{13}C NMR measurements were performed on a Varian XL 400 MHz instrument using tetramethylsilane as the reference. X-band EPR spectra were collected on a Bruker EMX spectrometer with an ER041XG microwave bridge and ER4102ST cavity; samples were held in a liquid N_2-filled finger Dewar.

The purity of the ligands and quantification of 3,5-di-*tert*-butylcatechol, 3,5-di-*tert*-butylquinone, and 2,4-di-*tert*-butyl phenolate were assessed by ^{1}H-NMR or GC-MS on an HP 5970 GC-MS equipped with an AT-5 (ALLTECH) column and mass selective detector, or on an HP 5890 GC equipped with a HP-DB1 column and FID detector, relative to an internal standard (mesitylene).

Synthesis of [(DBED)$_2$Cu$_2$(O$_2$)](X)$_2$—A 0.5 mM solution of [(DBED)$_2$Cu$_2$(O$_2$)](X)$_2$ was prepared by injecting a 200 μL solution of [(DBED)Cu(MeCN)](X) (25 mM, THF) into a precooled (193 K), O_2 (1 atm) saturated solution (5 mL) of CH_2Cl_2, acetone, THF, MeTHF, or toluene. The following data is for [(DBED)$_2$Cu$_2$(O$_2$)](CF$_3$SO$_3$)$_2$. 1H NMR (CD$_2$Cl$_2$, 193 K, 400 MHz): δ 1.18 (s, 36H, *tert*-Bu), 2.05 (s, 24H, MeCN), 2.61 (s, 4H), 2.67 (s, 4H). UV-vis (λ_{max} nm (ε, M^{-1} cm^{-1}), THF): 350 (36,000), 485 (1,200), 605 (900). EPR (77 K, MeTHF): silent.

Synthesis of Intermediate A—A 0.5 mM solution of [[Cu(DBED)]$_2$(O$_2$)](CF$_3$SO$_3$)$_2$ (**P^{DBED}**) in THF was prepared by injecting 200 μL of a [LCu(MeCN)](CF$_3$SO$_3$) solution (25 mM, THF) into a pre-cooled (153 K), O_2-saturated 2MeTHF solution (5 mL). The bright-green species **A** was prepared by addition of 2.5–3 equivalents of sodium 2,4-di-*tert*-butyl-phenolate to the N_2-purged **PDBED** solution at 153 K. The reaction mixture was allowed to react for 60 seconds and then frozen in liquid N_2 for rR analysis. The solution is EPR silent at 77 K. UV-Vis (λ_{max} (ε, M^{-1} cm^{-1}), 2MeTHF): 295 (20,000), 418 (18,000), 630 (3,800).

Synthesis of Intermediate B—The light-brown species **B** was prepared by addition of 1–3 equiv of sodium 2,4-di-*tert*-butyl-phenolate to the **P^{DBED}** solution at 193 K, or by thermal decay of species **A** at 153 K. After the complete decay of species **A**, the solution was frozen in liquid N_2 and the sample used for rR analysis. The solution is EPR silent at 77 K. UV-Vis (λ_{max} (ε, M^{-1} cm^{-1}), 2MeTHF): 290 (16,000).

Synthesis of Intermediate C—The purple species **C** was prepared by addition of 1 equiv of a 100 mM H_2SO_4 solution in THF to a solution containing species **B** at 193 K. The solution was then frozen in liquid N_2 and the sample used for rR analysis. The solution is EPR silent at 77 K. UV-Vis (λ_{max} (ε, M^{-1} cm^{-1}), 2MeTHF): 290 (16,000), 550 (3,000).

Oxidation of Exogenous Substrates—A solution of [(DBED)$_2$Cu$_2$(O$_2$)](CF$_3$SO$_3$)$_2$ (5 mM, 5 mL) in THF (N_2 atmosphere, 193 K) was prepared from [(DBED)Cu(MeCN)](CF$_3$SO$_3$) and excess O_2. For anaerobic reactions, the excess O_2 was removed prior to addition of substrates by purging with N_2 for 15 min.

The reaction of 2,4-di-*tert*-butylphenolate was performed at 193 K in THF with excess O_2 removed. Addition of 1 equiv of substrate (0.05 mL, 50 mM solution in THF) changed the color from dark green to light yellow-green. After 15 min, the reaction was quenched with H_2SO_4 (0.5 M, 2 mL), and the solvent was removed under vacuum. The residue was extracted

with chloroform and analyzed by ^{1}H NMR and GC-MS. The amounts of phenol, catechol, and quinone were quantified by comparing with known mixtures of pure compounds. For ^{18}O-[(DBED)$_2$Cu$_2$(O$_2$)](CF$_3$SO$_3$)$_2$, the residue was analyzed by negative mode ESI-MS (Finnegan LCQ) to determine the ratio of ^{16}O/^{18}O products, revealing more than 80% ^{18}O incorporation.

Resonance Raman Spectroscopy—Laser excitation lines (provided by a Coherent Innova Sabre 25/7 Ar$^+$ or a Coherent I90C-K Kr$^+$ CW ion laser) were chosen to enhance and probe the copper-oxygen modes. Resonance Raman spectra were obtained using a Princeton Instruments ST-135 back-illuminated CCD detector on a Spex 1877 CP triple monochromator with 2,400, 1,800 and 1,200 grooves/mm holographic spectrograph grating. Spectral resolution was < 2 cm^{-1}. Sample spectra were collected at ~77 K with a liquid N$_2$-filled finger Dewar (Wilmad) that was hand-spun to minimize sample decomposition (at excitation energies > 458 nm) during collection. Typical rR sample concentrations were in the range of 2 to 5 mM of Cu to minimize self-absorption. Isotopic substitution was achieved by oxygenation with ^{18}O$_2$ (Icon, 99%).

Computational Details—All calculations were performed using the Gaussian03 Rev. D.01 or E.01 software suite.[58] Copper and oxygen atoms were treated with the

$$^1E = \frac{2^{BS}E - \langle S^2 \rangle_{BS} \, ^3E}{2 - \langle S^2 \rangle_{BS}}$$

(2)

Alrich's all-electron TZVP basis[59, 60] throughout. All other atoms were treated with the Pople split-valence 3−21+G* basis.[61–63] The B3LYP density functional[64–66] was also used throughout. Geometry optimizations were performed using restricted formalism. The default SCF convergence criteria and Berny optimization algorithm[67] were used throughout. Broken-symmetry single point calculations and population analyses were performed by first generating the high-spin wavefunction and using the *guess=(read,mix)* keyword to generate the unrestricted broken-symmetry singlet wavefunction. Wavefunction stability was confirmed using the *stable=opt* keyword. The broken-symmetry energies, given in Figures throughout the manuscript, were calculated using the spin-corrected method by Yamaguchi *et al.* given by Equation 2.[68] Time-dependent DFT calculations were performed using the default formalism in Gaussian03,[69–71] and the resulting UV-Vis spectra were calculated using the SWizard program, revision 4.4,[72] using the Gaussian model. The half-bandwidths, $\Delta_{1/2}$, of 3,100 cm^{-1}. Mulliken populations and Natural Bonding Orbital[73, 74] analyses were computed using the stabilized wavefunction for each structure. Molecular orbital coefficients were parsed and viewed using QMForge.[75] MO diagrams were constructed from G03 cube files using VMD[76] and the Tachyon ray tracer[77] routine. Normal modes were visualized using GaussView[78] and Molden.[79] Some 2-D PES surfaces were generated with gnuplot.

Supplementary Material

Refer to Web version on PubMed Central for supplementary material.

Acknowledgments

References

1. Solomon EI, Sundaram UM, Machonkin TE. Chem Rev 1996;96:2563–2605. [PubMed: 11848837]

2. Klinman JP. Chem Rev 1996;96:2541–2562. [PubMed: 11848836]

3. Solomon EI, Baldwin MJ, Lowery MD. Chem Rev 1992;92:521–542.

4. Solomon EI, Chen P, Metz M, Lee SK, Palmer AE. Angew Chem, Int Ed 2001;40:4570–4590.

5. Eickman NC, Solomon EI, Larrabee JA, Spiro TG, Lerch K. J Am Chem Soc 1978;100:6529–6531.

6. Hazes B, Magnus KA, Bonaventura C, Bonaventura J, Dauter Z, Kalk KH, Hol WG. Prot Sci 1993;2:597–619.

7. Klabunde T, Eicken C, Sacchettin JC, Krebs B. Nat Struct Biol 1998;5(12):1084–1090. [PubMed: 9846879]

8. Matoba Y, Kumagai T, Yamamoto A, Yoshitsu H, Sugiyama M. J Biol Chem 2006;281(13):8981–8990. [PubMed: 16436386]

9. Wilcox DE, Porras AG, Hwang YT, Lerch K, Winkler ME, Solomon EI. J Am Chem Soc 1985;107:4015–4027.

10. Winkler ME, Lerch K, Solomon EI. J Am Chem Soc 1981;103:7003–7005.

11. Mirica LM, Ottenwaelder X, Stack TDP. Chem Rev 2004;104(2):1013–1045. [PubMed: 14871148]

12. Lewis EA, Tolman WB. Chem Rev 2004;104:1047–1076. [PubMed: 14871149]

13. Cruse RW, Kaderli S, Meyer CJ, Zuberbühler AD, Karlin KD. J Am Chem Soc 1988;110(15):5020–5024.

14. Mirica LM, Vance M, Rudd DJ, Hedman B, Hodgson KO, Solomon EI, Stack TDP. J Am Chem Soc 2002;124(32):9332–9333. [PubMed: 12167002]

15. Mirica LM, Vance M, Rudd DJ, Hedman B, Hodgson KO, Solomon EI, Stack TDP. Science 2005;308:1890–1892. [PubMed: 15976297]

16. Mirica LM, Vance M, Rudd DJ, Hedman B, Hodgson KO, Solomon EI, Stack TDP. J Am Chem Soc 2006;128:2654–2665. [PubMed: 16492052]

17. Pidcock E, Obias HV, Zhang CX, Karlin KD, Solomon EI. J Am Chem Soc 1998;120(31):7841–7847.

18. Itoh S, Kumei H, Taki M, Nagatomo S, Kitagawa T, Fukuzumi S. J Am Chem Soc 2001;123:6708–6709. [PubMed: 11439064]

19. Palavincini S, Granata A, Monzani E, Casella L. J Am Chem Soc 2005;127:18031–18036. [PubMed: 16366554]

20. Santagostini L, Gullotti M, Monzani E, Casella L, Dillinger R, Tuczek F. Chem Eur J 2000;6:519–522.

21. Karlin KD, Haka MS, Cruse RW, Meyer GJ, Farooq A, Gultneh Y, Hayes JC, Zubieta J. J Am Chem Soc 1988;110(4):1196–1207.

22. Obias HV, Lin Y, Murthy NN, Pidcock E, Solomon EI, Ralle M, Blackburn NJ, Neuhold YM, Zuberbühler AD, Karlin KD. J Am Chem Soc 1998;120(49):12960–12961.

23. Kitajima N, Fujisawa K, Morooka T, Toriumi K. J Am Chem Soc 1989;111(24):8975–8976.

24. Karlin KD, Hayes JC, Gultneh Y, Cruse RW, McKown JW, Hutchison JP, Zubieta J. J Am Chem Soc 1984;106(7):2121–2128.

25. Murthy NN, Mahroof-Tahir M, Karlin KD. Inorg Chem 2001;40(4):628–635. [PubMed: 11225103]

26. Karlin KD, Tyeklàr Z, Farooq A, Haka MS, Ghosh P, Cruse RW, Gultneh Y, Hayes JC, Toscano PJ, Zubieta J. Inorg Chem 1992;31(8):1436–1451.

27. Halfen JA, Mahapatra S, Wilkinson EC, Kaderli S, Young VG, Cramer CJ, Que L Jr, Tolman WB. Science 1996;271:1397–1400. [PubMed: 8596910]

28. Cole AP, Mahadevan V, Mirica LM, Ottenwaelder X, Stack TDP. Inorg Chem 2005;44:7345–7364. [PubMed: 16212361]

29. Mahadevan V, DuBois JL, Hedman B, Hodgson KO, Stack TDP. J Am Chem Soc 1999;121:5583–5584.

30. Mahadevan V, Hou ZG, Cole AP, Root DE, Lal TK, Solomon EI, Stack TDP. J Am Chem Soc 1997;119:11996–11997.

31. Stack TDP. Dalton Trans 2003;10:1881–1889.

32. Cahoy J, Holland PL, Tolman WB. Inorg Chem 1999;38(9):2161–2168. [PubMed: 11671001]

33. Mahadevan V, Henson MJ, Solomon EI, Stack TDP. J Am Chem Soc 2000;122:10249–10250.

34. Eickman NC, Himmelwright RS, Solomon EI. Proc Nat Acad Sci 1979;76:2094–2098. [PubMed: 287049]

35. Baldwin MJ, Root DE, Pate JE, Fujisawa K, Kitajima N, Solomon EI. J Am Chem Soc 1992;114:10421.

36. Henson MJ, Vance M, Zhang CX, Liang HC, Karlin KD, Solomon EI. J Am Chem Soc 2003;125 (17):5186–5192. [PubMed: 12708870]

37. Pau MYM, Davis MI, Orville AM, Lipscomb JD, Solomon EI. J Am Chem Soc 2007;129:1944–1958. [PubMed: 17256852]

38. Schenk G, Pau MYM, Solomon EI. J Am Chem Soc 2004;126:505–515. [PubMed: 14719948]

39. Szilagyi RK, Metz M, Solomon EI. J Phys Chem A 2002;106:2994–3007.

40. Henson MJ, Mukherjee P, Root DE, Stack TDP, Solomon EI. J Am Chem Soc 1999;121(44):10332–10345.

41. Casella L, Monzani E, Gullotti M, Caragnino D, Cerina G, Santagostini L, Ugo R. Inorg Chem 1996;35:7516–7525.

42. Reim J, Krebs B. J Chem Soc Dalton Trans 1997;(20):3793–3804.

43. Lynch MW, Valentine M, Hendrickson DN. J Am Chem Soc 1982;104:6982–6989.

44. Strufkens DJ, Snoeck TL, Lever ABP. Inorg Chem 1988;27:953–956.

45. Gordon DJ, Fenske RF. Inorg Chem 1982;8:2907–2915.

46. Stack TDP. Unpublished results

47. Streitweiser AJ, Jagow RH, Fahey RC, Suzuki S. J Am Chem Soc 1958;80:2326–2332.

48. Stack TDP. To date there has been no experimental evidence (i.e. EXAFS) that a Cu(I) species is generated.

49. Becker M, Schindler S, Karlin KD, Kaden TA, Kaderli S, Palanché T, Zuberbühler AD. Inorg Chem 1999;38(9):1989–1995. [PubMed: 11670976]

50. Cruse RW, Kaderli S, Karlin KD, Zuberbühler AD. J Am Chem Soc 1988;110(20):6882–6883.

51. Karlin KD, Nasir MS, Cohen BI, Cruse RW, Kaderli S, Zuberbühler AD. J Am Chem Soc 1994;116 (4):1324–1336.

52. Suzuki K, Shimokawa C, Morioka C, Itoh S. Biochem 2008;47:7108–7115. [PubMed: 18553939]

53. Morioka C, Tachi Y, Suzuki S, Itoh S. J Am Chem Soc 2006;128:6788–6789. [PubMed: 16719449]

54. Matoba Y, Kumagai T, Yamamoto A, Yoshitsu H, Sugiyama M. J Biol Chem 2006;281(13):8981–8990. [PubMed: 16436386]

55. Op't Holt BT, Dustman J, Solomon EI. ChemTracts Inorg Chem 2006;19(11):435–444.

56. Kubas GJ, Monzyk B, Crumbliss AL. Inorg Synth 1979;19:90–92.

57. Mandal S, Macikenas D, Protasiewicz JD, Sayre LM. J Org Chem 2000;65:4804–4809. [PubMed: 10956455]

58. Frisch, MJ.; Trucks, GW.; Schlegel, HB.; Scuseria, GE.; Robb, MA.; Cheeseman, JR.; Montgomery, JJA.; Vreven, T.; Kudin, KN.; Burant, JC.; Millam, JM.; Iyengar, SS.; Tomasi, J.; Barone, V.; Mennucci, B.; Cossi, M.; Scalmani, G.; Rega, N.; Petersson, GA.; Nakatsuji, H.; Hada, M.; Ehara, M.; Toyota, K.; Fukuda, R.; Hasegawa, J.; Ishida, M.; Nakajima, T.; Honda, Y.; Kitao, O.; Nakai, H.; Klene, M.; Li, X.; Knox, JE.; Hratchian, HP.; Cross, JB.; Adamo, C.; Jaramillo, J.; Gomperts, R.; Stratmann, RE.; Yazyev, O.; Austin, AJ.; Cammi, R.; Pomelli, C.; Ochterski, JW.; Ayala, PY.; Morokuma, K.; Voth, GA.; Salvador, P.; Dannenberg, JJ.; Zakrzewski, VG.; Dapprich, S.; Daniels, AD.; Strain, MC.; Farkas, O.; Malick, DK.; Rabuck, AD.; Raghavachari, K.; Foresman, JB.; Ortiz, JV.; Cui, Q.; Baboul, AG.; Clifford, S.; Cioslowski, J.; Stefanov, BB.; Liu, G.; Liashenko, A.; Piskorz, P.; Komaromi, I.; Martin, RL.; Fox, DJ.; Keith, T.; Al-Laham, MA.; Peng, CY.; Nanayakkara, A.; Challacombe, M.; Gill, PMW.; Johnson, B.; Chen, W.; Wong, MW.; Gonzalez, C.; Pople, JA. Gaussian 03, D.01; E.01. Gaussian, Inc; Wallingford, CT: 2004.

59. Schaefer A, Horn H, Alrichs R. J Chem Phys 1992;97(4):2571–2577.

60. Schaefer A, Huber C, Alrichs R. J Chem Phys 1994;100(8):5289–5835.

61. Binkley JS, Pople JA, Hehre WJ. J Am Chem Soc 1980;102(3):939–947.

62. Gordon MS, Binkley JS, Pople JA, Pietro WJ, Hehre WJ. J Am Chem Soc 1982;104(10):2797–2803.

63. Pietro WJ, Francl MM, Hehre WJ, Defrees DJ, Pople JA, Binkley JS. J Am Chem Soc 1982;104(19): 5039–5048.

64. Becke AD. J Chem Phys 1993;98(2):5648–5652.

65. Lee C, Yang W, Parr RG. Phys Rev B 1988;37(2):785–789.

66. Miehlich B, Savin A, Stoll H, Preuss H. Chem Phys Lett 1989;157(3):200–206.

67. Schlegel HB. J Comp Chem 1982;3(2):214–218.

68. Yamaguchi K, Jensen F, Dorigo A, Houk KN. Chem Phys Lett 1988;149(5–6):537–542.

69. Bauernschmitt R, Alrichs R. Chem Phys Lett 1996;256:454–464.

70. Casida ME, Jamorski C, Casida KC, Salahub DR. J Chem Phys 1998;108(11):4439–4449.

71. Stratmann RE, Scuseria GE, Frisch MJ. J Chem Phys 1998;109(19):8218–8224.

72. Gorelsky, SI. SWizard Program 4.4. University of Ottawa; Ottawa, Ontario, Canada: 2008.

73. Carpenter JE, Weinhold F. J Mol Struct (Theochem) 1988;46:41–62.

74. Foster JP, Weinhold F. J Am Chem Soc 1980;102(24):7211–7218.

75. Tenderholt, AL. QMForge, 2.1. Stanford University; Stanford, CA, USA: 2008.

76. Humphrey W, Dalke A, Schulten K. J Molec Graphics 1996;14:33–38.

77. Stone, J. Tachyon Ray Tracer, 0.97. Rolla; MO, USA: 2007.

78. Dennington, IR.; Todd, K.; Millam, JM.; Eppinnett, K.; Hovell, WL.; Gilliland, R. GaussView, 3.09. Semichem, Inc; Shawnee Mission, KS, USA: 2003.

79. Schaftenaar G, Noordik JH. J Comput-Aided Mol Des 2000;14:123–134. [PubMed: 10721501]
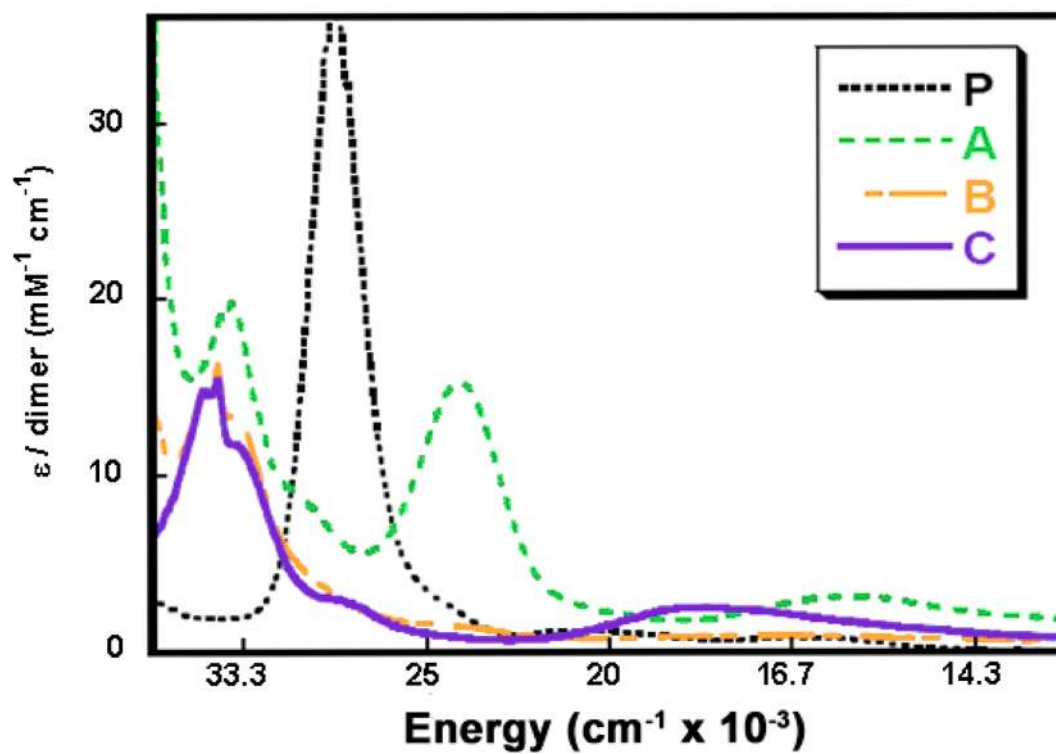
Figure 1.
The electronic absorption spectra of **P**^{DBED}, **A**, **B**, and **C**.
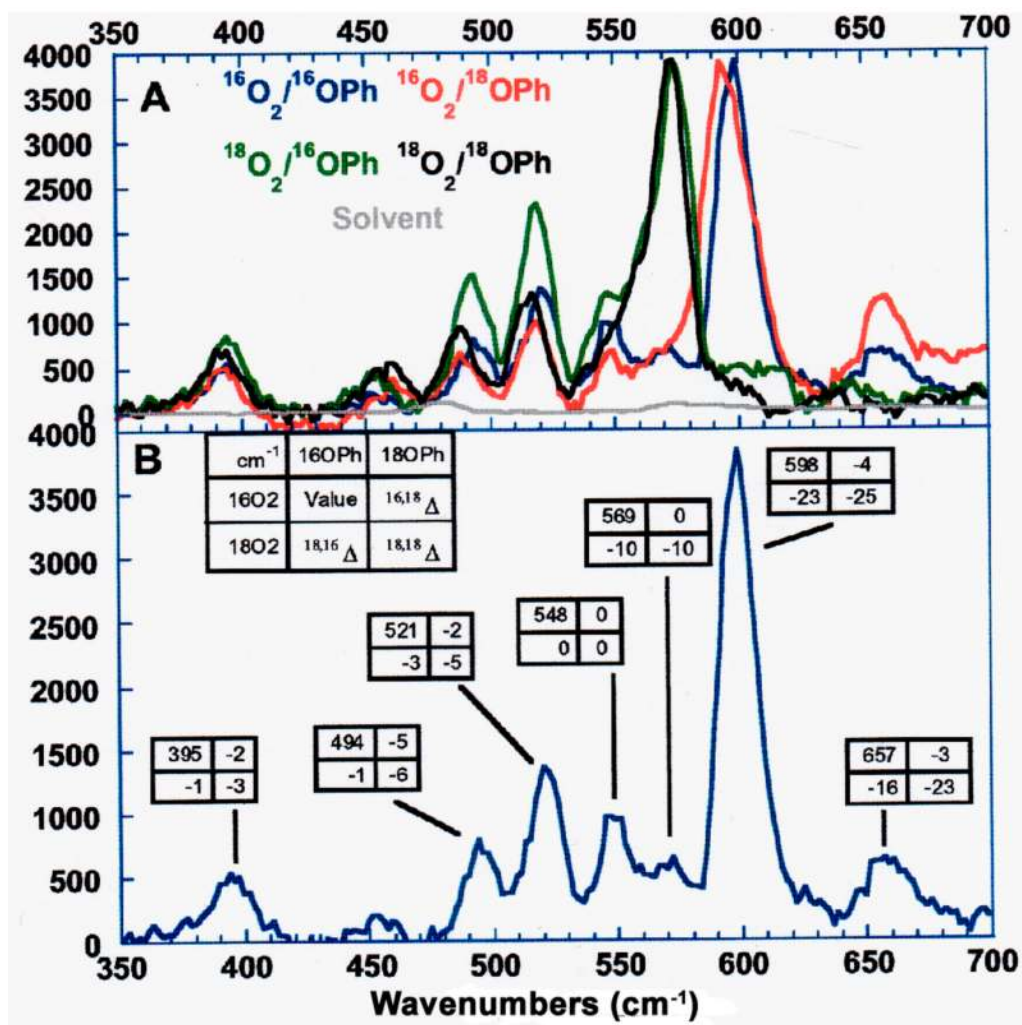
Figure 2.
A) rR spectra of **A** with ^{16}O and ^{18}O substituted phenolate and ^{16}O and ^{18}O substituted dioxygen in THF/2-MeTHF at 77 K with 413 nm excitation. **B)** Solvent subtracted $^{16}O/^{18}O$ substituted phenolate spectrum of **A** at 77 K with isotope shifts labeled.
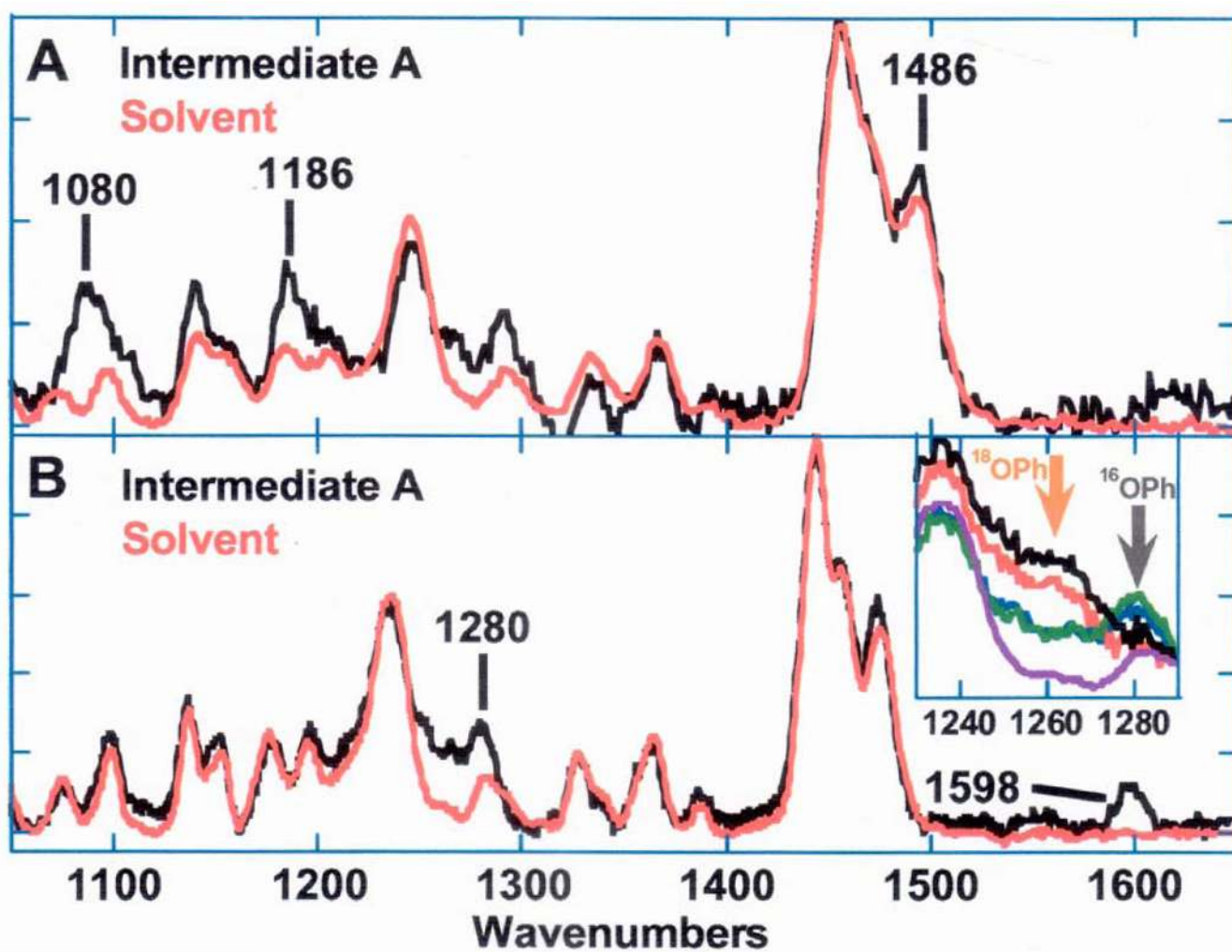
Figure 3.
rR spectrum of **A** at 77 K with $^{16}O/^{18}O$ substituted phenolate in THF/2-MeTHF **A)** 413 nm excitation **B)** 650 nm excitation. Inset: rR with 600 nm excitation showing isotopic shift of 1,280 cm^{-1} vibration.
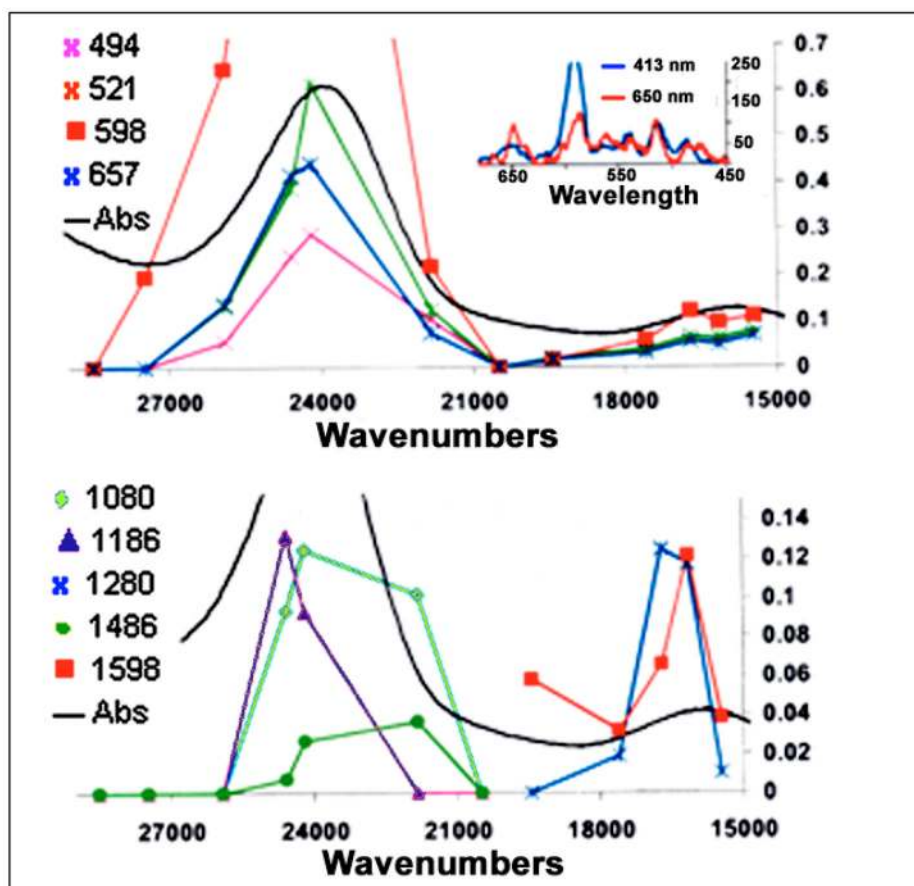
Figure 4.
rR profiles of **A. Top)** Cu-L modes. Inset shows relative intensity of 598 cm^{-1} vibration with 413 and 650 nm excitation. **Bottom)** Phenolate aromatic ring modes showing that different ring modes are enhanced in the two absorption features.
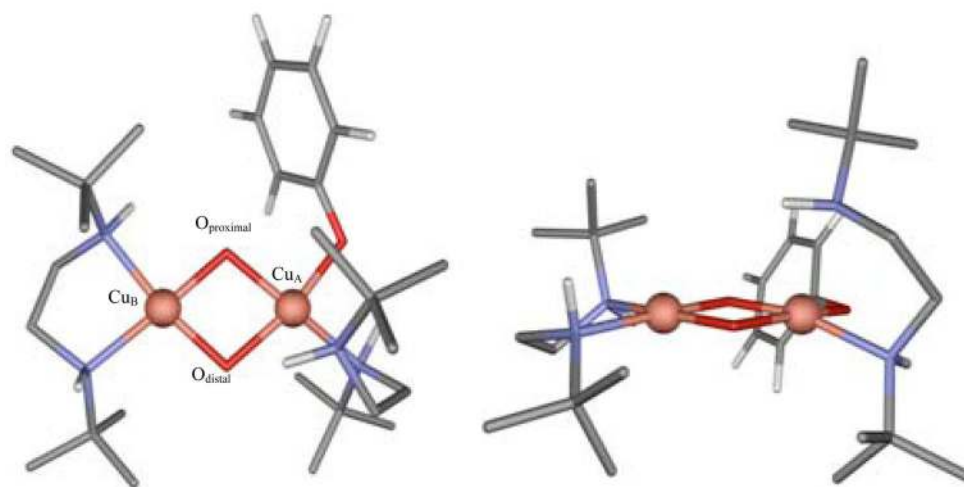
Figure 5.
DFT optimized structure of **A** in which the *tert*-butyl substituents of the phenolate are replaced with a hydrogen atom. Two views are shown to visualize the orientation of the phenolate ring relative to the Cu_2O_2 core. Selected metrical parameters are given in Table 5 (*vide infra*).
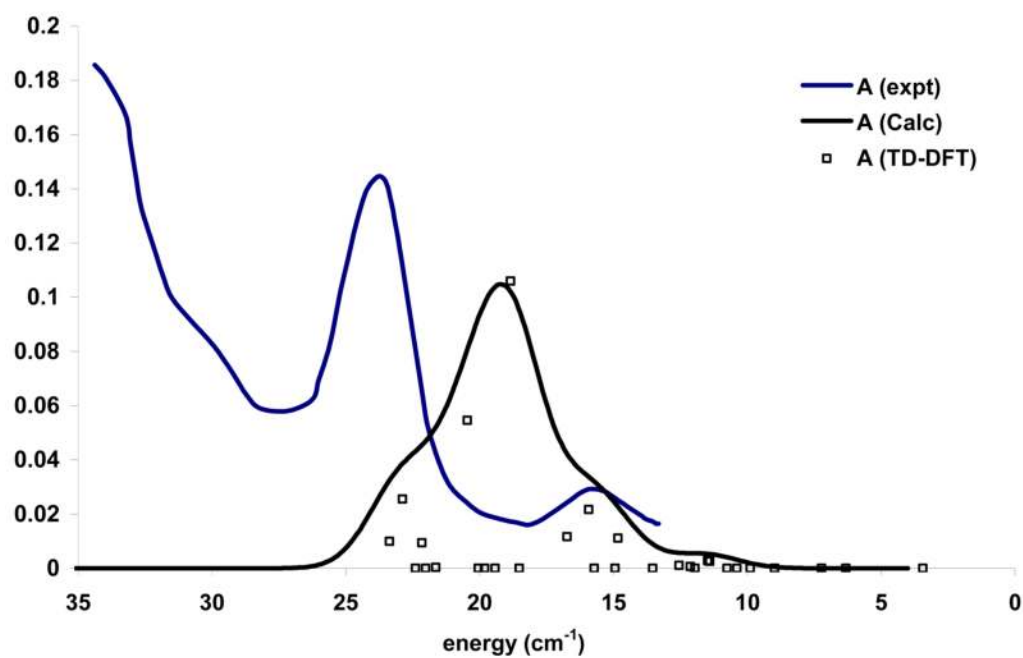
Figure 6.
The simulated spectrum of **A** (black) overlaid with the experimental electronic absorption spectrum of **A** (purple), in arbitrary absorbance units. The boxes represent TD-DFT-predicted transitions within **A** in units of oscillator strength.
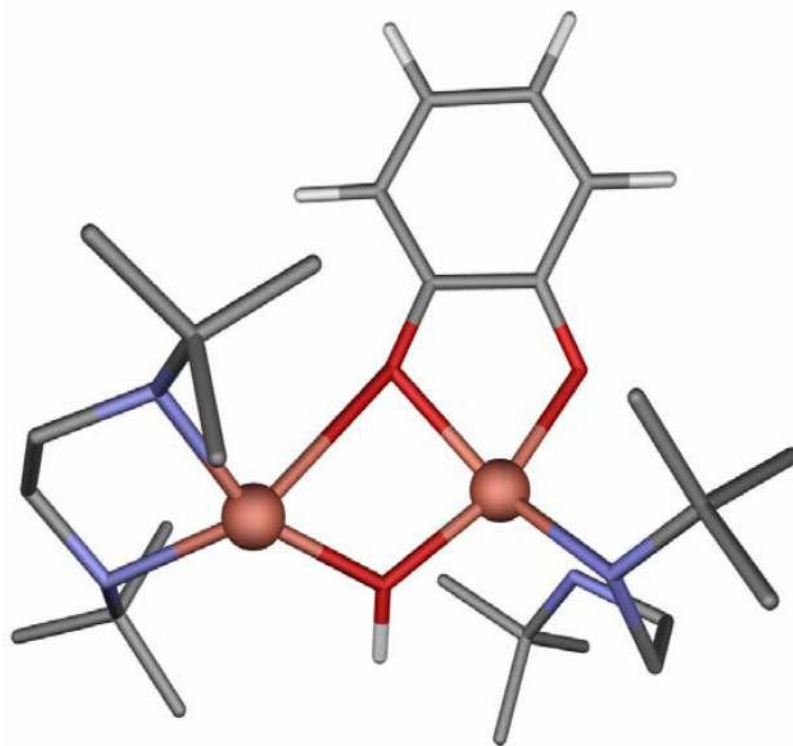
Figure 7.
Proposed structure of **B**, a catecholate asymmetrically bound to two a.f.-coupled Cu(II) ions, bridged by a hydroxyl- group. In this computational model, the *tert*-butyl substituents of the experimental system have been substituted with hydrogens.
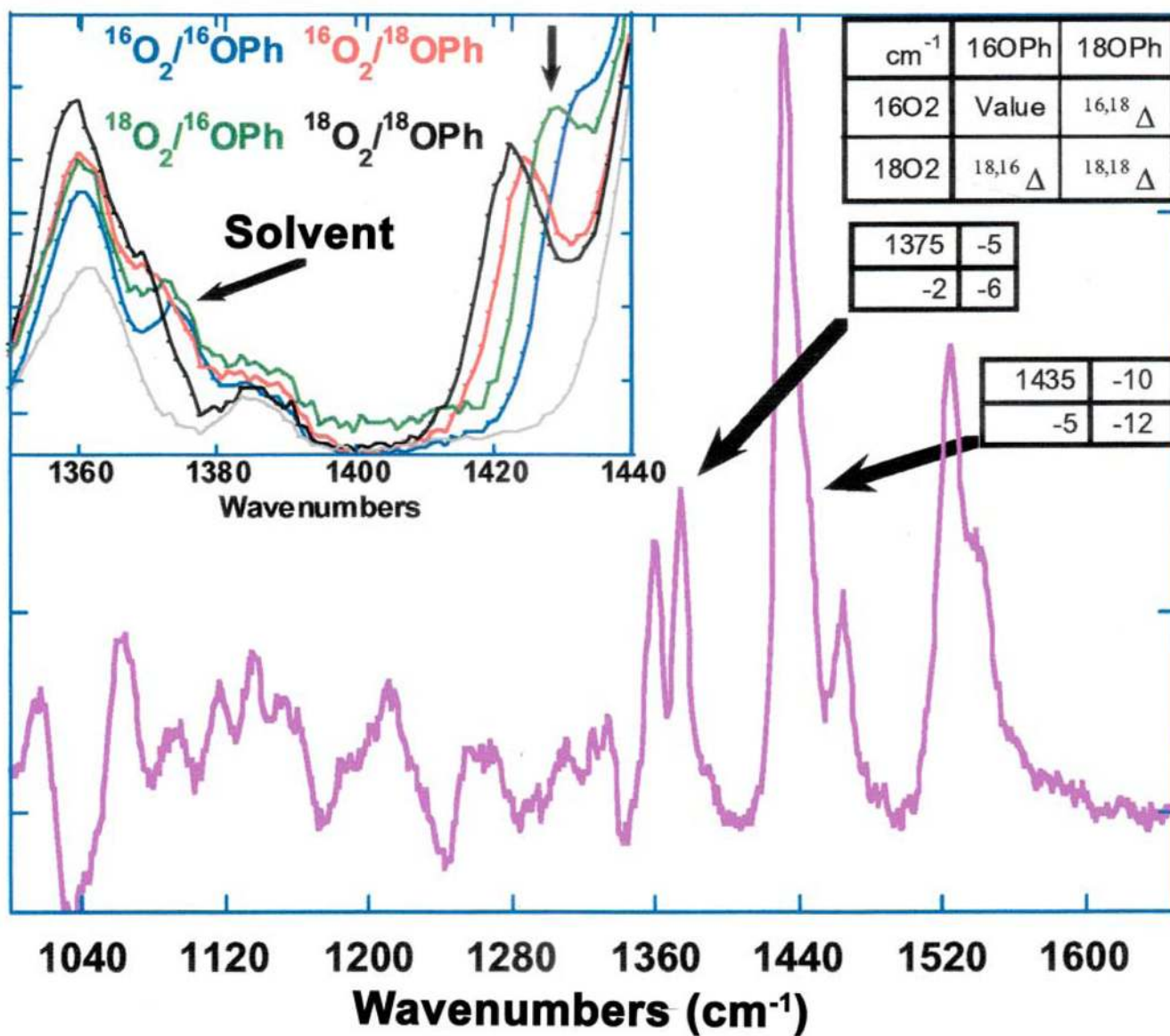
Figure 8.
Solvent subtracted rR spectrum (high-energy region) of **C** with 530 nm excitation in THF/2-MeTHF at 77 K. Inset: rR spectrum of **C** with ^{16}O and ^{18}O substituted phenolate and O_2 in THF/2-MeTHF at 77 K.
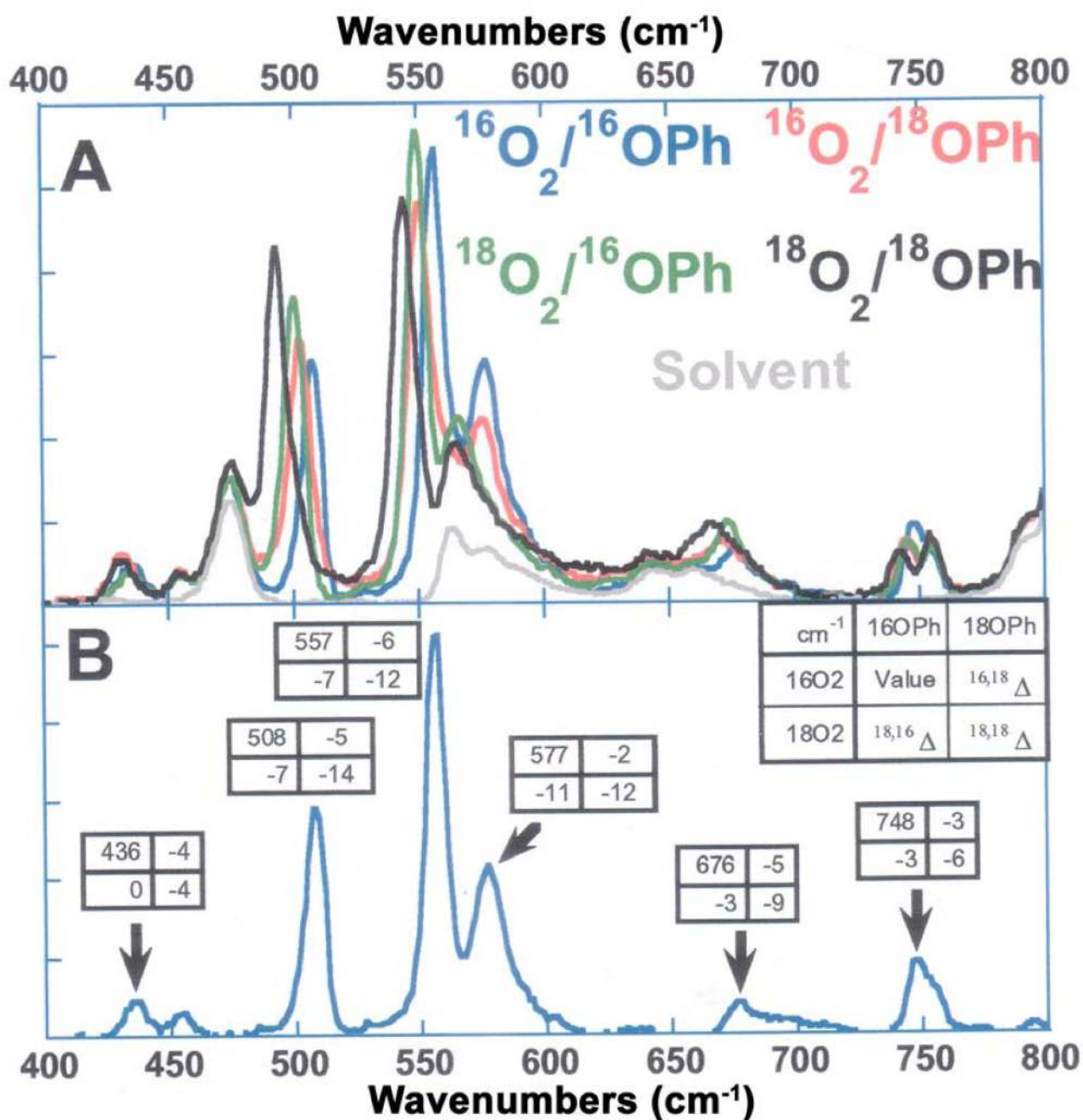
Figure 9.
rR spectra of **C** with 530 nm excitation at 77 K. **A)** [16]O and [18]O substituted phenolate and O_2 in THF/2-MeTHF. **B)** Solvent subtracted spectra of **C** with isotope shifts labeled.
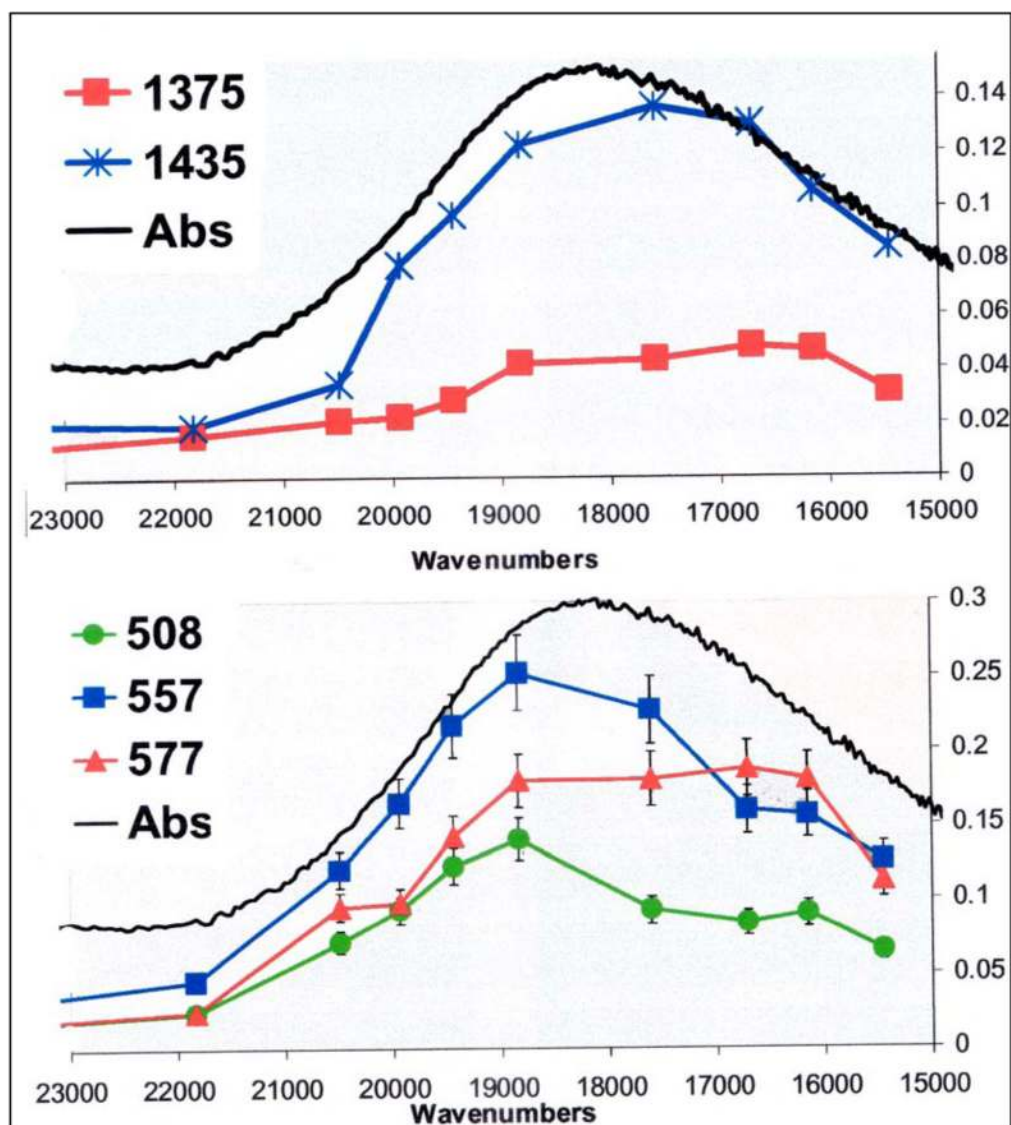
Figure 10.
rR profiles of **C. Top)** ν_{C-O} modes. **Bottom)** Selected Cu-L modes with ±10% error bars.
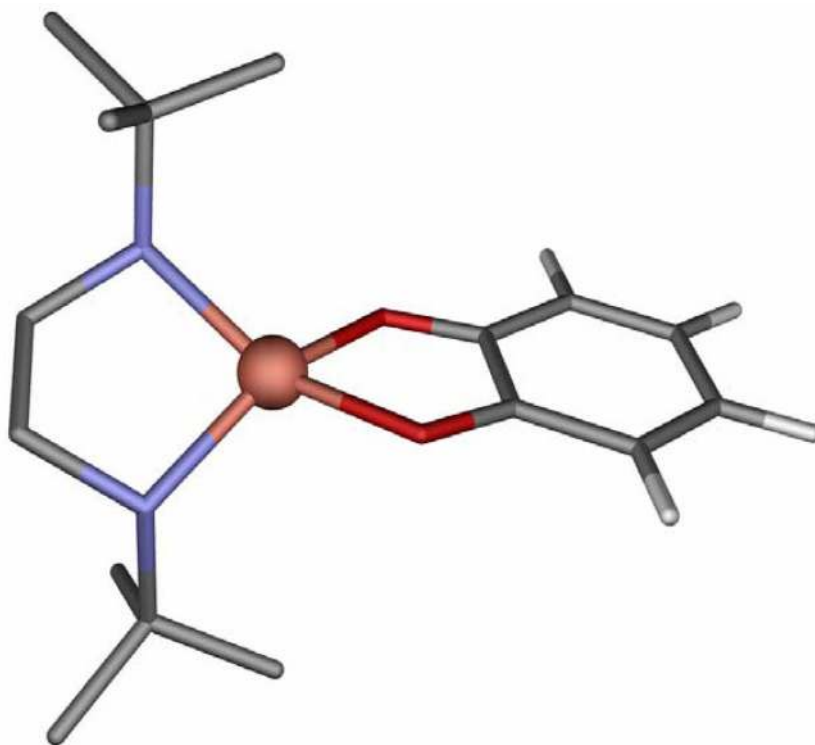
Figure 11.
The DFT-optimized structure of a minimal model of **C**. Note the torsional angle of the semiquinone relative to the CuN_2 plane. In this computational model, the *tert*-butyl substituents of the experimental system have been substituted with hydrogens.
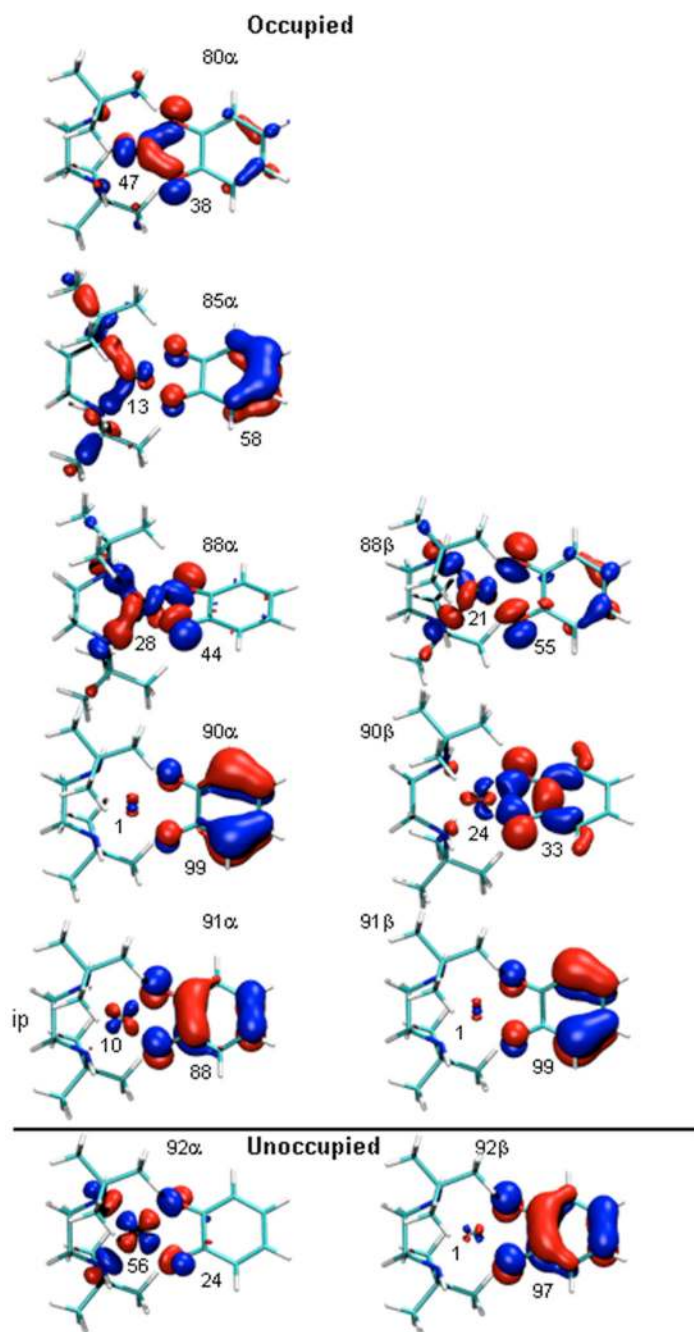
Figure 12.
Selected α and β molecular orbitals of **C** revealing it as an a.f.-coupled Cu(II) semiquinone complex and showing orbitals involved in TD-DFT-predicted CT transitions. Shown next to the Cu ion and ring are the MO coefficients for each orbital. The number next to the ring represents the total contribution from all 12 atoms in the ring ($C_6H_4O_2$)
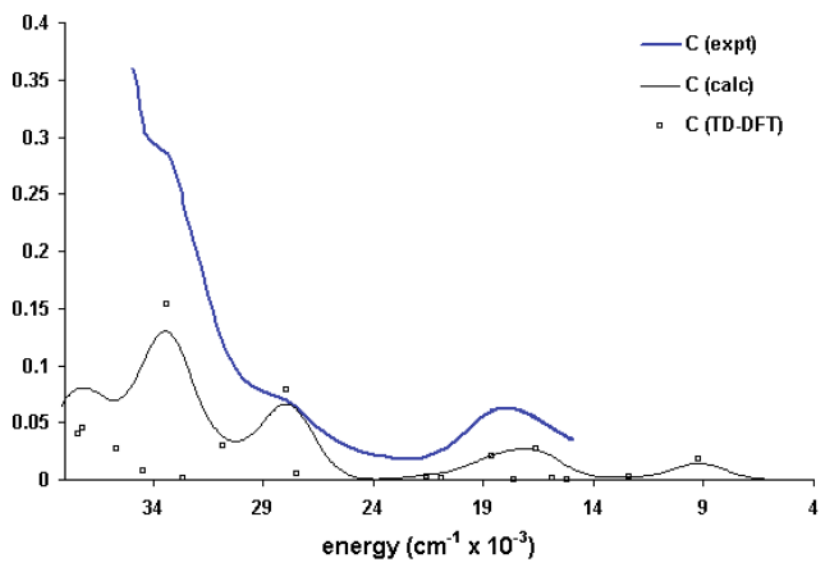
Figure 13.
The simulated absorption spectrum of **C** (black) overlaid with the experimental absorption spectrum of **C** (purple) in arbitrary absorption units. The boxes indicated TD-DFT-calculated transitions. Oscillator strengths are on the same scale here as in the TD-DFT plot of **A** in Figure 6.
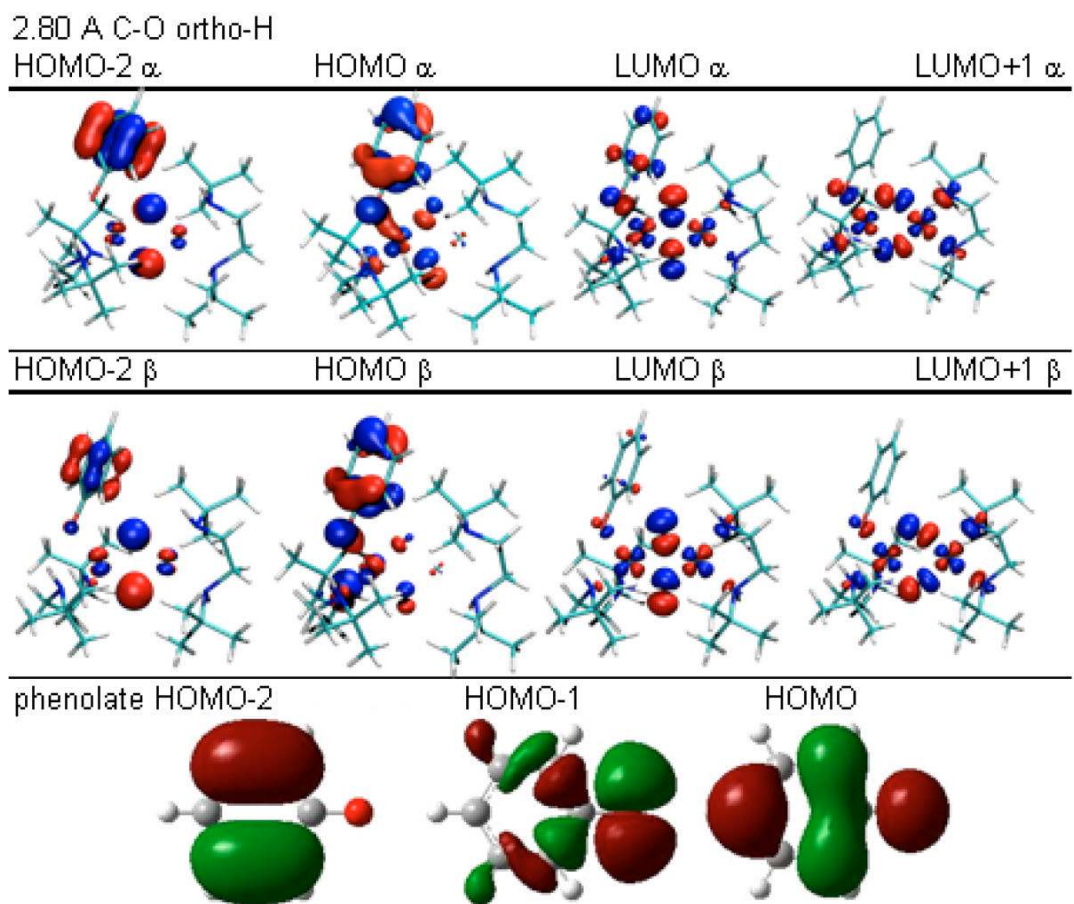
Figure 14.
α and β molecular orbitals for the DFT optimized structure of **A**. Shown for reference are normal phenolate orbitals. In both α and β manifolds, both Cu $d_{x^2-y^2}$ are unoccupied, confirming the ions as Cu(III) and the ring HOMO is a phenolate HOMO. The α and β ring-based HOMO align with the oxo-based α and β LUMO in a configuration priming the *ortho*-C for attack by the proximal O.
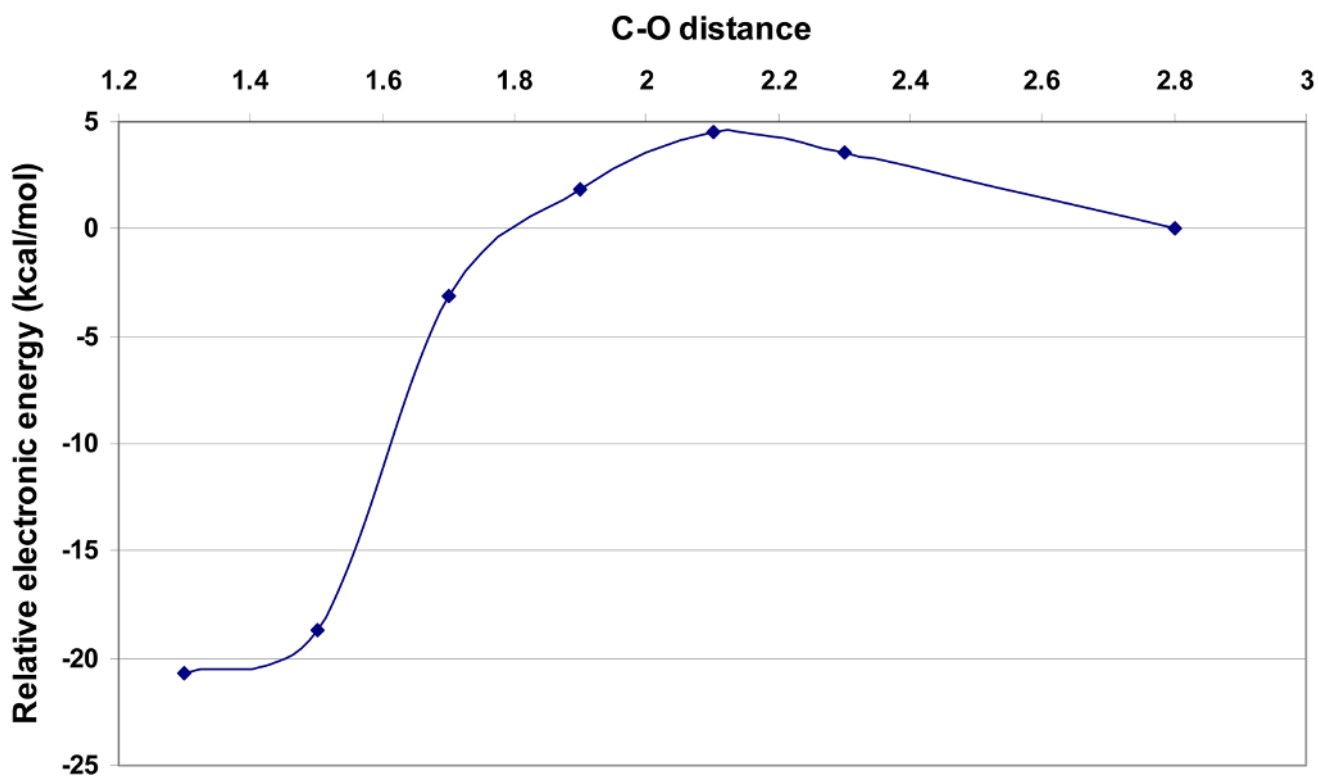
Figure 15.
The potential energy surface of the gas-phase reaction coordinate of phenolate with the DBED dicopper(II) complex made by gradually reducing the *ortho*-C to $O_{proximal}$ distance.
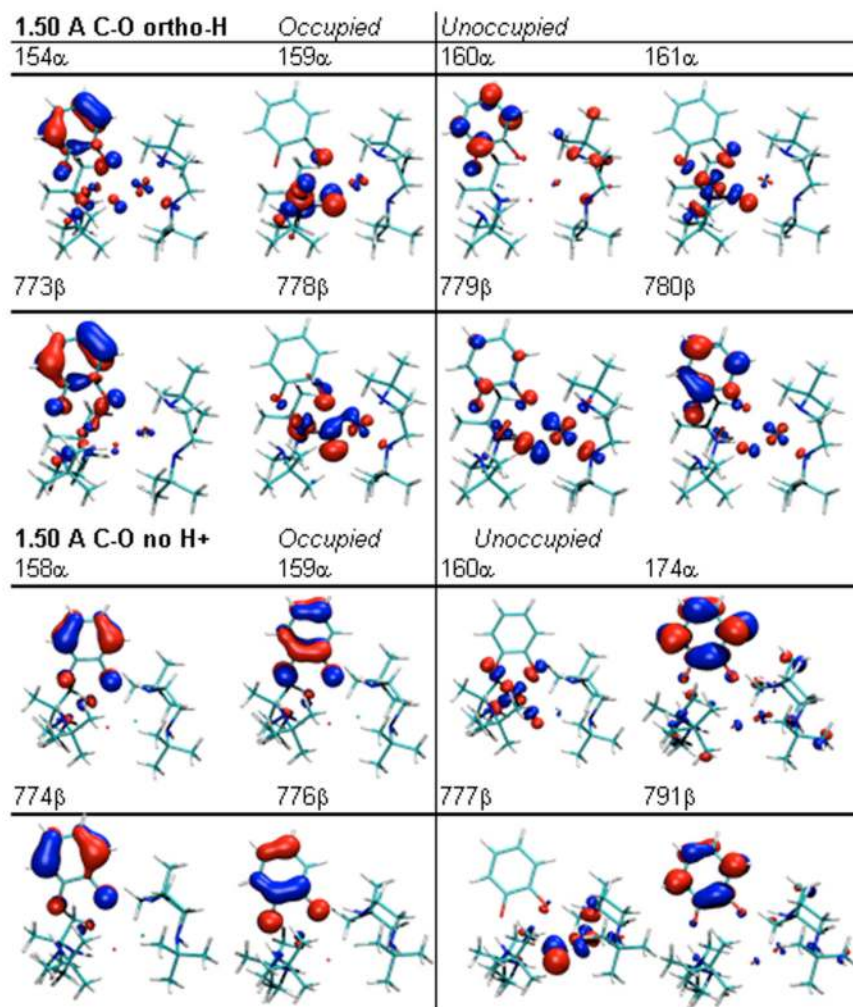
Figure 16.
Molecular orbitals of the 1.50 Å C-O distance systems are compared for a system with an intact *ortho*-C-H bond and that of a system with a cleaved *ortho*-C-H bond. The appearance of the catecholate-like orbitals in the two highest occupied orbitals of the system on the bottom indicates that C-O bond formation occurs if the *ortho*-C-H bond has dissociated.
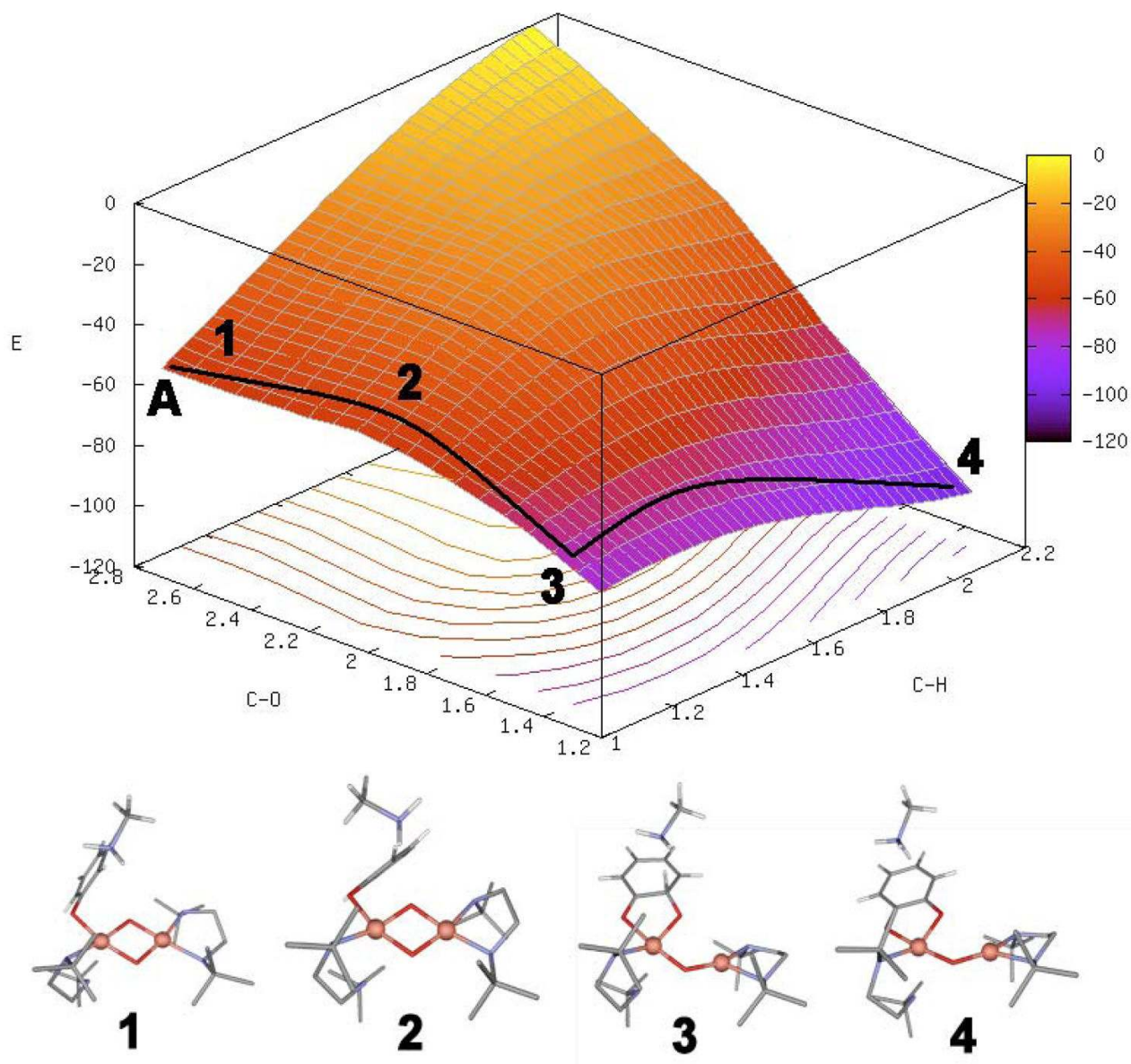
Figure 17.
2-D potential energy surface showing electronic energy changes versus C-O and C-H distances. Structure **1** represents the starting structure, **A**. The dark line indicates the lowest energy route on the PES, traversing the energy barrier near d(C-O) ~ 2.10 Å (**2**), followed by spontaneous proton transfer to an exogenous base to reach the lowest energy part of the surface. Protonation of O_{distal} via the exogenous base produces **B** 25.5 kcal/mol lower in energy than the structure at **4**.

1.30 C-O distance/ 2.07 C-H distance; CH$_3$NH$_3^+$ 1.30 C-O distance/ distal OH$^-$; CH$_3$NH$_2$ 1.30 C-O distance/ "distal" OH$_2$
Relative Energy (kcal/mol)   0.00   -25.5   -218
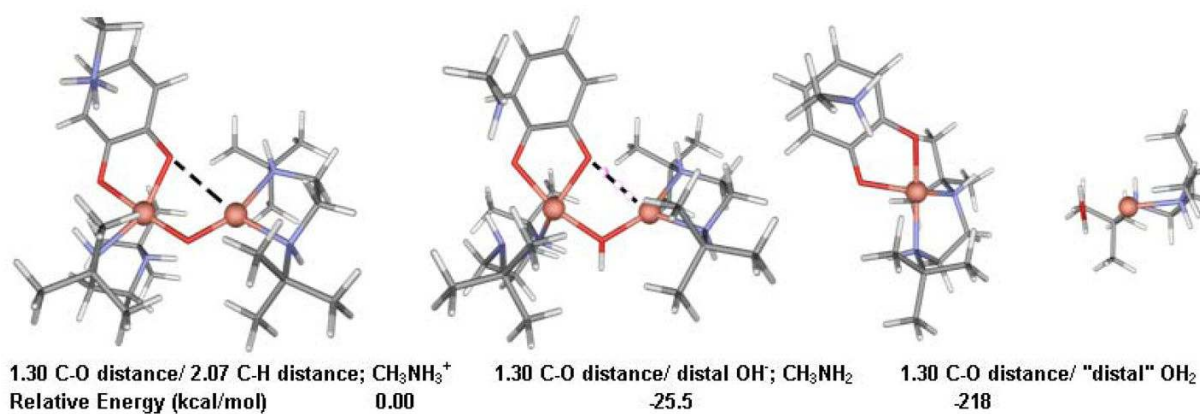
Figure 18.
Structures and relative energies of three structures with *ortho*-C-O$_{proximal}$ distances of 1.30 Å in which the C-H bond has dissociated. **Left)** protonated methylamine **Middle)** protonated O$_{diatal}$, proton transferred via exogenous base; proposed structure of **B Right)** Addition of one proton creates "distal" OH$_2$ followed by reduction of one Cu and dissociation of dimer; creation of a proposed a.f.-coupled Cu(II)-semiquinone; proposed structure of **C**
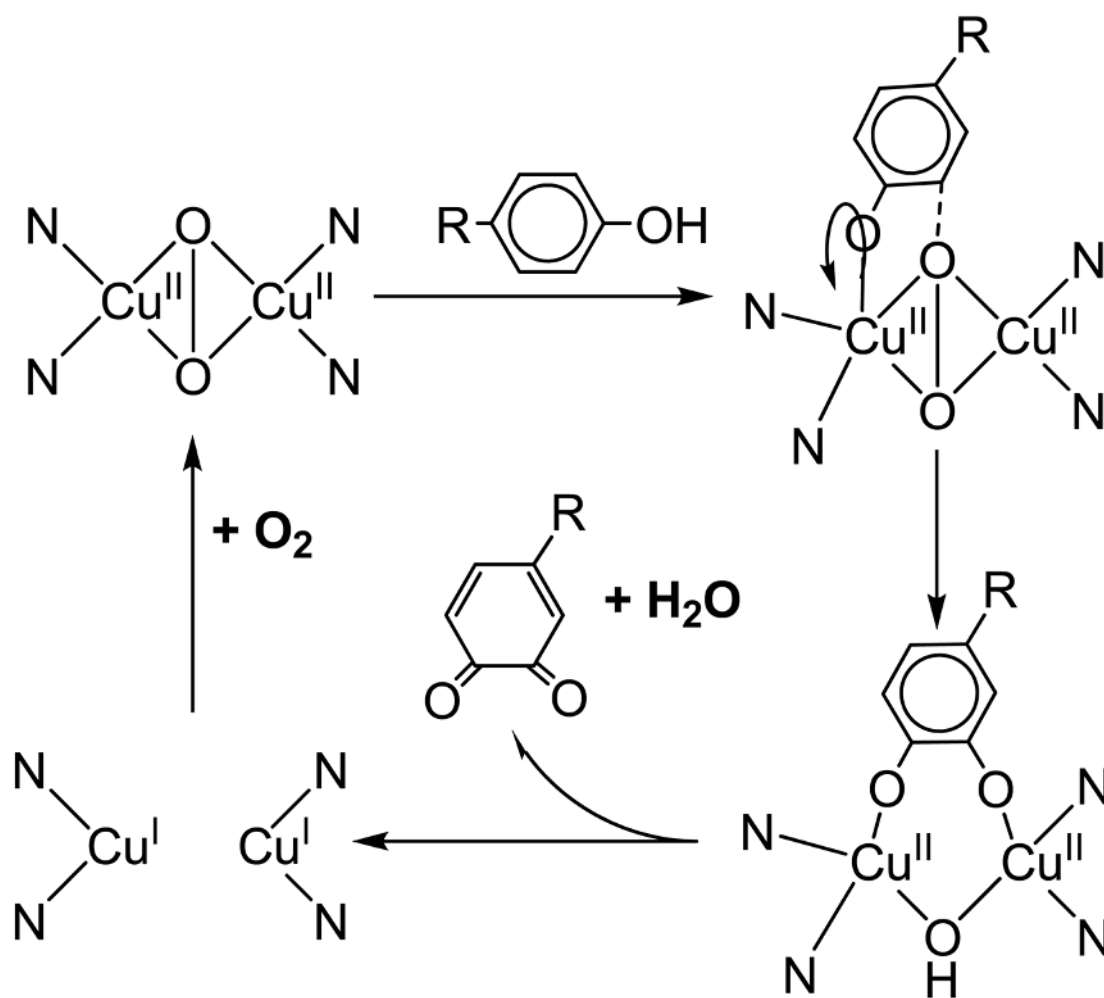
Scheme 1.
The experimentally-derived mechanism for the hydroxylation reaction of tyrosinase. N represents His ligation from the protein and one such ligand has been omitted from each Cu for clarity. The arrow on the O in step 2 denotes rearrangement of the phenolate into the equatorial plane. Adapted from reference 1.
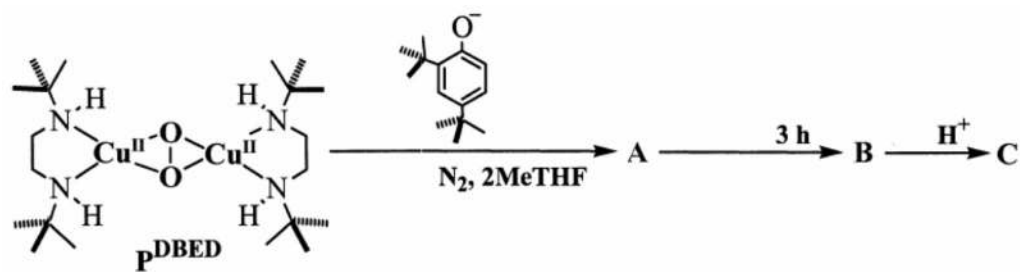
Scheme 2.
The reaction between **P^{DBED}** and 2,4-di-*tert*-butylphenolate at 153 K, with the formation of **A**, **B**, and **C**.
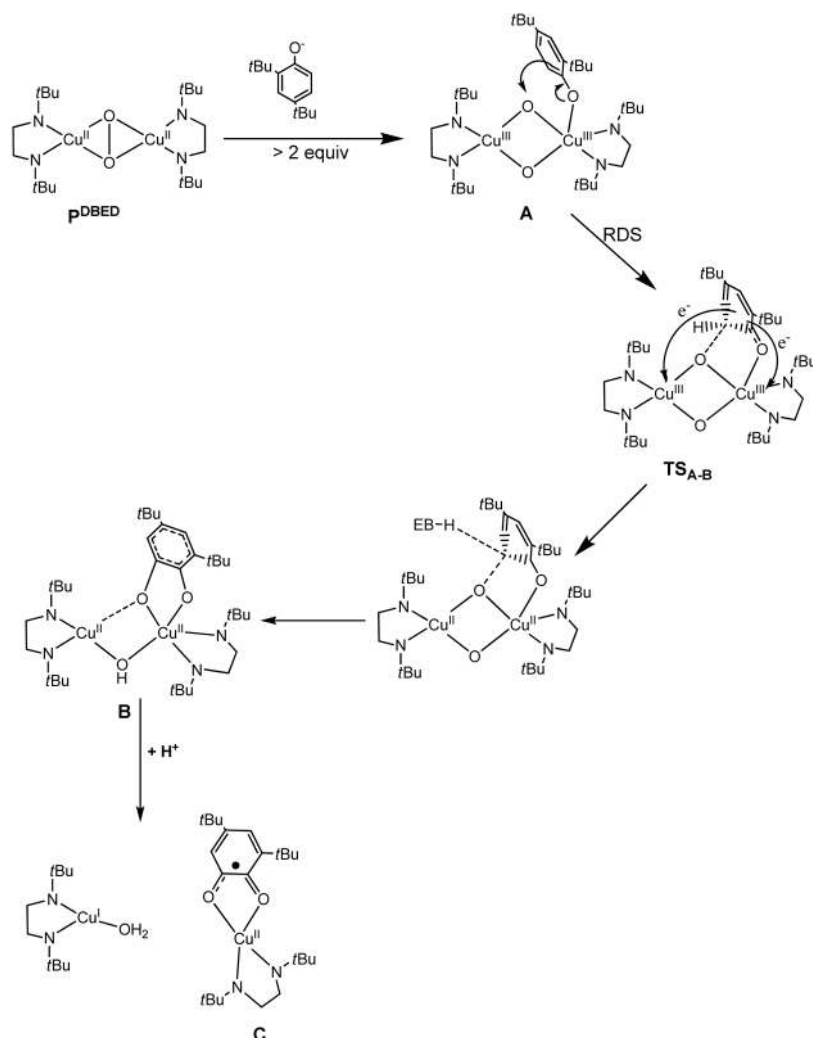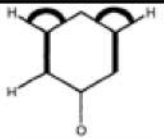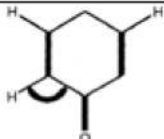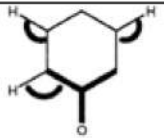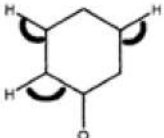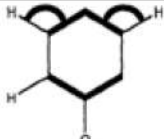
Scheme 3.
The spectroscopically and computationally derived mechanism for the reaction of **P^DBED** with 2,4-di-*tert*-buylphenolate via intermediates **A**, **B**, and **C**. The rate-limiting step of the reaction occurs between **A** and **B**. EB represents an exogenous base. **Step 1)** phenolate binds to one Cu and rearranges toward the equatorial plane as indicated by the curved arrow. **Step 2)** The rate limiting step involves distortion of the *ortho*-C to sp^3 and double-oxidation of the phenolate in the electrophilic attack upon the ring by the proximal oxide. **Step 3)** Transfer of *ortho*-H$^+$ to nearby exogenous base. **Step 4)** First protonation of O$_{distal}$ via exogenous base and the formation of catecholate. **Step 5)** Addition of one proton creates a Cu(II)-semiquinone monomer and a Cu(I) monomer as the dimer dissociates.

Table 1

Phenolate normal mode distortions and assignments. Dark lines on the left indicate bonds and angles involved in the mode. DFT-calculated distortions are shown on the right. Red lines indicate bond shortening and blue lines bond elongation relative to phenolate in the ground state.

Enhanced Region (cm⁻¹)	ν_{obs} (cm⁻¹)	Ring Mode	Atomic Motion	Calculated Distortion
15,400	1,598	v8a vC=C		
15,400	1,280	v7a vC-O		π_{op}
23,800	1,486	v19a		
23,800	1,186	v9a		
23,800	1,080	v18		π_{ip}

Table 2

Top) Potential phenolate binding geometries and Cu-L modes for a mono- or bis-phenolate bonded bis-μ-oxo dicopper(III) core. **Middle)** Normal modes of vibration for the Cu_2O_2 core in different point groups and experimental and calculated rR shifts and isotope effects upon $^{18}O_2$ and/or $^{18}OPh^-$ substitution. Experimental values are in parentheses, NCA-predicted values are in normal font, and DFT-predicted values are in italics. **Bottom)** DFT core-distortion upon binding of a single phenolate, reflected in the DFT structure of **A**.
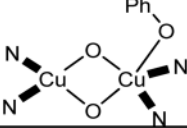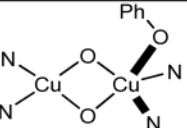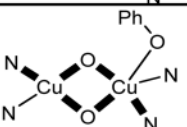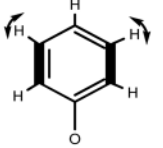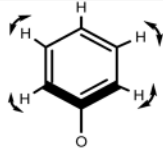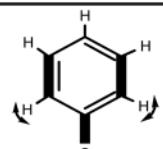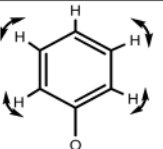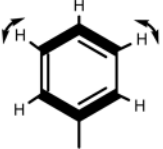
Species	Point Group	Distortion
trans-bis-phenolate 1 A_g Cu-L mode	C_{2h}	
cis-bis-phenolate 1 A_1 Cu-L mode	C_{2v}	
mono-phenolate All A' Cu-L modes	C_s	

D_{2h}	C_{2h}	C_{2v}	C_s	Atomic Motion	(Exp) NCA Calc	$^{18}O_2$ ^{16}OPh	$^{16}O_2$ ^{18}OPh	$^{18}O_2$ ^{18}OPh
B_{3u}	B_u	B_1	A'		(657) 643.9 *658*	(-16) -29.3* *-11*	(-3) - *-2*	(-23) - *-12*
B_{1g}	A_g	B_1	A'		(-) 625.9 *650*	(-) -30.1* *-*	(-) - *-*	(-) - *-*
A_g	A_g	A_1	A'		(598) 611.5 *601*	(-23) -28.1* *-9*	(-4) - *-8*	(-25) - *-20*
B_{2u}	B_u	A_1	A'		(569) 549.9 *517*	(-10) -25.0* *-2*	(0) - *0*	(-10) - *-2*
PhO⁻ predicted distortion								

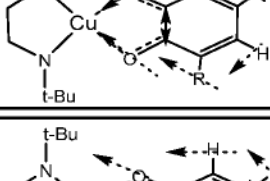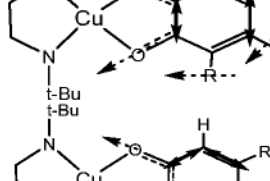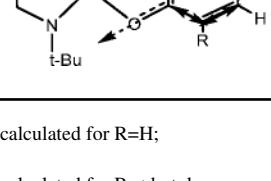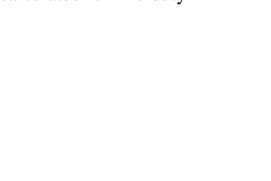*J Am Chem Soc.* Author manuscript; available in PMC 2009 November 13.
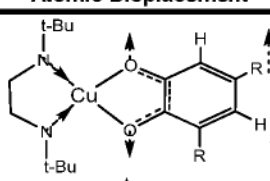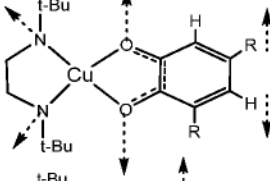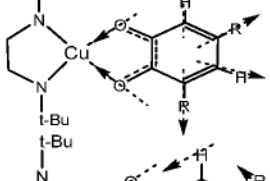
Table 3

Calculated vibrational Cu-L and intraligand modes for the computational model of **A** including isotope shifts upon $^{18}O_2$ and/or ^{18}OPh substitution compared to rR-observed vibrations of **A**. Bold lines and arrows denote stretching and bending motions, respectively.

Atomic Motion	(Exp) Calc	Isotope shifts $^{18}O_2$ ^{16}OPh	$^{16}O_2$ ^{18}OPh	$^{18}O_2$ ^{18}OPh
	(395) 403	(-1) -4	(-2) -10	(-3) -11
	(494) 458	(-1) -2	(-5) -12	(-6) -13
	(521) 515	(-3) -11	(-2) -2	(-5) -12
	(1598) 1598	- -	- -	- -
	(1486) 1512	- -	- -	- -
	(1280) 1282	- -2	(-20) -11	(-20) -11
	(1186) 1208	- -	- -	- -
	(1080) 1035	- -	- -	- -

Table 4

Normal modes and calculated frequency shifts (in cm^{-1}) of a model of **C** with isotopic shifts upon $^{18}O_2$ and/or $^{18}OPh^-$ substitution. Experimentally observed values are in parentheses. Arrows indicate in-plane displacement vectors, except for H in the top two modes which indicate antisymmetric out-of-plane H bending.

Atomic Displacement	Normal Mode	(Exp) Calc^a Calc^b	$^{18}O_2$ ^{16}OPh	$^{16}O_2$ ^{18}OPh	$^{18}O_2$ ^{18}OPh
	mixed chelate ν_{Cu-N} ring op H bend	(508) 500 518	(-7) -3 -5	(-5) -3 -5	(-14) -10 -12
	mixed chelate ν_{Cu-N} ring op H bend	(557) 521 563	(-7) -7 -5	(-6) -7 -4	(-12) -8 -9
	mixed ν_{Cu-O} ring	(577) 607 593	(-11) -7 -12	(-2) -6 -6	(-12) -8 -17
	mixed ν_{Cu-O} ring	(748) 758 -	(-3) -7 -	(-3) -7 -	(-6) -13 -
	mixed $R\nu_{C-O}$ ring C-C	(1375) 1393 1367	(-2) -13 -9	(-5) -13 -2	(-6) -19 -10
	mixed ν_{C-O} ring C=C	(1435) 1487 1393	(-5) -1 -2	(-10) -1 -7	(-12) -2 -10

^{a}calculated for R=H;

^{b}calculated for R=t-butyl

Table 5

Selected parameters from the geometry optimized structure of **A**.

parameter		distance (Å)
d(Cu-Cu)		2.82
d(O-O)		2.35
d(Cu-OPh)		1.88
d(prox O - o -C)		2.80
d(Cu-O)avg		1.84
ring:Cu_2O_2 torsion		74.7°
$Cu_{phenolate}$	ρ_{spin}	0.095
Cu_{distal}	ρ_{spin}	−0.058

Table 6

Mayer's Bond Order for the *ortho*-C–O$_{proximal}$ bond and Mulliken charge on the *ortho*-H as the distance between the aromatic ring and O$_{proximal}$ is varied.

ortho -C - O$_{proximal}$ (Å)	MBO	charge *o* -H$^+$
2.8	0.297	0.245
2.3	0.346	0.273
2.1	0.398	0.287
1.9	0.515	0.309
1.7	0.841	0.316
1.5	1.148	0.346
1.3	1.104	0.321

Table 7

Mayer's Bond Order for the *ortho*-C–O$_{proximal}$ interaction along the 2-D reaction coordinate including methylamine as a proton acceptor. Shown for comparison are the MBO for the phenolate C-O bond.

Structure	Mayer's Bond Order	
d(C-O)/d(C-H)	O$_{prox}$-*ortho* -C	O$_1$-C$_1$
2.80/1.08	0.306	0.690
2.30/1.08	0.265	0.924
2.10/1.08	0.322	1.082
1.90/1.10	0.510	1.316
1.70/1.10	0.575	1.698
1.30/1.15	1.101	1.400
1.30/1.58	1.351	1.253
1.30/2.09	1.538	1.264